TAMPEREEN TEKNILLINEN YLIOPISTO
TAMPERE UNIVERSITY OF TECHNOLOGY

TOPI UUSITALO

DESIGN AND CHARACTERIZATION OF NOVEL DISTRIBUTED FEEDBACK LASER STRUCTURES FOR DIFFERENCE FREQUENCY GENERATION

Master of Science thesis

Examiners: Docent Mihail Dumitrescu
and D.Sc. (Tech.) Antti Laakso
Examiners and topic approved by the
Faculty Council of the Faculty of
Natural Sciences
on 13th August 2014

ABSTRACT

TOPI UUSITALO: Design and characterization of novel distributed feedback laser structures for difference frequency generation
Tampere University of Technology
Master of Science thesis, 57 pages
January 2015
Master of Science (Tech.) Degree Programme in Science and Engineering
Major: Engineering Physics
Examiners: Docent Mihail Dumitrescu and Doctor of Science (Tech.) Antti Laakso
Keywords: distributed feedback, edge emitting semiconductor laser, dual-wavelength radiation, difference frequency generation, tunable laser, optimization

The high frequency signals from difference frequency generation (DFG) have found several promising and interesting applications in the recent years. This has promoted great interest in the design of the sources for DFG. However, compact, efficient, tunable and cheap sources are still not commonplace. These kind of sources would have many use scenarios in various applications.

This thesis covers the design and characterization of novel dual-wavelength distributed feedback laser diodes (DFB-LD). The emphasis is on the laser structure and its properties in order to generate DFG. The applications of DFG such as radio-over-fiber (RoF) and terahertz radiation are also covered.

The basic theory for the simulation and design process is presented, as well as the theory related to the application areas. The implementations for both the simulations and the characterization process are presented in detail. The most important results from both numerical and characterization studies are presented and discussed. Some possible future directions for laser development and applications are further outlined.

TIIVISTELMÄ

TOPI UUSITALO: Uusien hajautetusti takaisinkytkettyjen laser-rakenteiden suunnittelu ja karakterisointi erotaajuusgenerointiin
Tampereen teknillinen yliopisto
Diplomityö, 57 sivua
Tammikuu 2015
Teknis-luonnontieteellinen koulutusohjelma
Pääaine: Teknillinen fysiikka
Tarkastajat: yliop. tutk. Mihail Dumitrescu ja tutk. toht. Antti Laakso
Avainsanat: hajautettu takaisinkytkentä, reunasta emittoiva puolijohdelaser, kaksoisaallonpituussäteily, erotaajuusgenerointi, viritettävä laser, optimointi

Erotaajuusgeneraatiosta saataville korkeataajuussignaaleille on ilmaantunut useita lupaavia ja mielenkiintoisia sovellutuskohteita lähivuosina. Tämä on aiheuttanut suurta kiinnostusta erotaajuusgeneraatiolähteitä kohtaan. Kompaktit, energiatehokkaat, viritettävät ja edulliset lähteet erotaajuusgenerointiin eivät kuitenkaan vielä ole yleisiä. Tällaisilla lähteillä olisi lukuisia käyttökohteita eri sovellutuksissa.

Tämä työ käsittelee uusien kaksoisaallonpituuksellisten hajautetun takaisinkytkennän laserien suunnittelua ja karakterisointia. Painotus on laser-rakenteella ja sen ominaisuuksissa erotaajuusgeneraation kannalta. Erotaajuusgeneraation sovelluksia, kuten kuidun yli toimivaa radiota ja terahertsisäteilyä käsitellään myös.

Simuloinnin ja suunnittelutyön taustan perusteoria esitellään, kuten myös sovellutuskohteisiin liittyvä teoria. Sekä simulointi- että karakterisointiprosessin toteutus esitellään yksityiskohtaisesti. Sekä numeeristen tutkimusten että karakterisoinnin tuloksista esitellään ja käsitellään tärkeimmät. Joitakin laser-kehityksen ja -sovellutusten mahdollisia tulevaisuuden suuntia on myös kirjattu.

FOREWORD

This thesis summarizes some of the results I have obtained in the fields of laser modelling, simulation, characterization, and other related areas in the past few years. The work was done at the Optoelectronics Research Center of Tampere University of Technology. The funding has been project based, in programs such as the Seventh Framework Programme of CORDIS and TUTLI of Tekes.

First I give my thanks to the director of ORC Dr. Pekka Savolainen for the possibility of working at ORC with novel and interesting research and development topics. Second thanks are for my supervisor, Docent Mihail Dumitrescu, for his insight into the direction of this thesis, as well as constructive and fruitful criticism. Third, I extend my thanks to all the people at ORC I've had the pleasure of working with, especially to Dr. Antti Laakso and Heikki Virtanen for the numerous interesting discussions about the topics in this thesis, to Dr. Jukka Viheriälä for his insight and expertise in the laser fabrication process, and to Antti Aho and Joel Salmi for the advice, direction and insight in fabrication and characterization of the lasers.

Lastly, most importantly, I want to let my family and friends know that without their friendship, support, understanding, and patience, this thesis would not have been completed in the spirit it was now. My warmest thanks to you all.

In Tampere, 17.12.2014

Topi Uusitalo

TABLE OF CONTENTS

SYMBOLS

α_0	Unperturbed gain
α_{int}	Internal losses
α_k	Dimensionless gain slope at frequency ω_k
α_{m}	Mirror losses
α	Net absorption coefficient
A_t	Transmission gain coefficient for the backward propagating wave
β	Complex propagation constant
β_0	Bragg propagation constant
β_i	Imaginary part of the β
θ_{jk}	Cross- or self-saturation coefficient between modes j and k
β_n	Self-saturation coefficient
β_r	Real part of the β
C	Coupling parameter
C_{jk}	Overlap factor between modes j and k
C_k	Overlap factor of mode k with itself
$\Delta\alpha$	Optical loss difference between a lasing mode and a competing mode
$\Delta\alpha_l$	Optical loss difference between two lasing modes
δ	Detuning factor
Δf	Peak frequency deviation
δ_{jk}	Dirac delta-function
$\Delta\nu$	Spectral linewidth
$\Delta\omega$	Difference angular frequency
E	Wave amplitude
$\mathbf{E}$	Time harmonic with angular frequency ω
E_c	Wave evolution in the coupled wave formalism
$E_i(x,y)$	Transverse mode profile of a lasing mode
ϵ_0	Vacuum permittivity
E_{tot}	Total incident field
F	Optical field flatness inside the laser cavity
f_{diff}	Difference frequency between two longitudinal modes

f_i	Optimization goal function
$\mathfrak{F}$	Optimization fitness function
g	Optical gain
γ	Filling factor
Γ	Shorthand for the coupled wave formalism
$\hat{\Gamma}$	Shorthand for the coupled wave formalism
g_L	Linear gain
$\hbar$	Reduced Planck constant
f_m	Modulation frequency
h	Frequency modulation index
$\mathbf{H}$	Cavity matrix including end facet reflections in the coupled wave TMM
i	Imaginary Unit
I_{avg}	Average field intensity in the laser cavity
η_{int}	Intensity overlap of two cavity field distributions
I_{tot}	Intensity for the total electric field
$I(z)$	Field intensity in the laser cavity at point z
k	Wave number
k_0	Propagation constant in vacuum
κ	Coupling coefficient
κ_g	Coupling coefficient due to gain variations
κ_i	Coupling coefficient due to n variations
κL	Grating coupling strength
L	Cavity length
Λ	Grating period
λ	Wavelength
λ_C	Central wavelength of a grating
M	Number of mirror pairs
m	Grating order
$\mathbf{M}$	Cavity matrix in the fundamental TMM formulation
μ	Transition dipole moment
n	Refractive index
n_0	Unperturbed refractive index
n_{eff}	Effective refractive index

$n_{\text{eff}}^{\text{tun}}$	Tuned effective refractive index
n_g	Effective group index
$\tilde{n}$	Complex effective refractive index
ν	Frequency
Ω	Non-zero residual corrugation phase at z=0
ω	Angular frequency
ω_0	Frequency of the dominant mode
Ω_{jk}	Frequency difference between modes j and k
ω_k	Frequency of the mode k
π	The ratio of circle's circumference to its diameter
R	Coupled wave propagating in the opposite direction of S
R	Cavity reflection coefficient
r_{it}^x	Amplitude reflection coefficient for x–polarized light from side i to t
ρ	Shorthand for the coupled wave formalism
$\mathbf{R}$	General reflection matrix in the fundamental TMM, or facet reflection matrix in the coupled wave TMM
S	Coupled wave propagating in the opposite direction of R
σ	Attenuation constant
τ_c	Intraband relaxation time
τ_{in}	Intraband relaxation time
τ_ν	Intraband relaxation time
T	Cavity transmission coefficient
t_{it}^x	Amplitude transmission coefficient for x–polarized light from side i to t
θ_i	Incident angle
θ_k	Amount of phase shift from a $\mathbf{P}$ matrix
θ_{jk}	Cross-saturation coefficient
θ_t	Transmission angle
$\mathbf{P}$	Phase shift matrix in the coupled wave TMM
$\mathbf{T}$	Propagation matrix in the fundamental TMM, or transfer matrix in the coupled wave TMM

w_i	Optimization goal function weight
ξ	Tuning magnitude
$\mathbf{x}$	Vector of design parameters
$\mathbf{Y}$	Cavity matrix without end facet reflections in the coupled wave TMM

ABBREVIATIONS

AM	Amplitude modulation
AR	Anti-reflection
BWA	Bang-bang weighted aggregate
CO	Central office
COD	Catastrophic optical damage
CPR	Carrier-photon resonance
CWA	Conventional weighted aggregate
DFB	Distributed feedback
DFG	Difference-frequency generation
DML	Dual-mode laser
DPS	Distributed phase shifts
DWA	Dynamic weighted aggregate
EEL	Edge-emitting laser
EHF	Extremely high frequency
ESA	Electrical spectrum analyzer
EU	End user
FM	Frequency modulation
GL	Gain lever
HF	High frequency
HR	High reflection
LD	Laser diode
LO	Local oscillator
MISO	Multiple in, single out
MLD	(Normalized) mode loss difference
MMF	Multi-mode fiber
MMW	Millimetre wave
OSA	Optical spectrum analyzer
PD	Photodiode
PPG	Pulse pattern generator
PPR	Photon-photon resonance
PS	Phase shift
PSO	Particle swarm optimization
RN	Remote node

BS	Base station
RoF	Radio-over-fiber
SHB	Spatial hole burning
SLM	Single longitudinal mode
SMF	Single-mode fiber
SMLD	(Normalized) side mode loss difference
SMSR	Side mode suppression ratio
TEC	Thermo-electric cooler
THz	Terahertz radiation
TMM	Transfer matrix method
TW	Traveling wave

1. INTRODUCTION

This thesis presents a novel approach to achieve high quality dual-wavelength emission from monolithic semiconductor lasers. Two wavelengths have been traditionally used in difference frequency generation (DFG) [1], but have also promising applications in sensing [2], radio-over-fiber (RoF) [3], and data transmission. A particular application of DFG with dual wavelength lasers is the generation of terahertz radiation (THz) [4]. Despite its several medical, security, and military applications, THz is notoriously difficult to generate and tune over certain frequency ranges.

The emphasis of the work reported in this thesis is on the theoretical part of various aspects of dual-wavelength laser operation and modeling. Since it is essential that the modeling and simulation results are validated, the thesis includes the most important measurement and characterization findings alongside the simulation studies. The correlation between the simulations and the measurements validates the models, and provides feedback on how well the fabricated devices correspond to the design.

Chapter 2 presents the relevant theoretical background to lasers and modeling, as well as the basics of some application areas of dual-mode lasers (DMLs). Chapter 3 gives details of the model implementation in the simulation software. Chapter 4 presents characterization studies performed on the fabricated lasers. Chapter 5 compares the most important simulation and experimental results and discusses the accuracy of the models and the fabrication process.

2. THEORY

This chapter summarizes the relevant principles and formulae for the models used in the thesis. Several methods have been developed for understanding the impact of structural variables, such as materials and dimensions, on the semiconductor laser operation and characteristics. They are founded on the basic principles, but the amount of approximations varies. In addition to the methods, this chapter describes the used approximations, mainly related to the phenomena involved in the new laser designs. Some DFG and dual-wavelength laser applications are also outlined.

2.1 Basic Principles

Stimulated emission [5] is the cornerstone of laser emission. To achieve this, population inversion [6, p. 5] is needed. This means that the energy levels above the ground level have more electrons than the ground level. Such a state appears in nature only momentarily (recently the possibility of exploiting these natural states has been studied [7]). In practice a pumping mechanism is needed: transferring electrons to an upper energy state by external energy injection. Pumping can be done for example by optical means by an external pump laser or, in the case of p-n junction laser, by electrical pumping. Figure 2.1 gives an illustration of basic laser nomenclature related to stimulated emission.

Pumping is not enough, the pumped material should also have a direct band-gap [8]: if the minima and the maxima of the conduction and the valence bands are not in the same position in the Brillouin zone, a phonon is required in addition to the recombining electron and hole in order to fulfill momentum conservation. This decreases the transition efficiency considerably and hampers stimulated emission. Single element semiconductors (both from group IV: C, Si, Ge, and Sn and from group VI: S, Se, and Te) have an indirect bandgap, but direct bandgaps are acievable by using compound semiconductors (III-V, II-VI, I-VI, I-VII, IV-VI, and II-V). A lot of research effort [9] has gone into engineering semiconductor alloys to achieve direct band gaps suited for various applications.

Stimulated emission requires high photon densities. To achieve this, the laser struc-

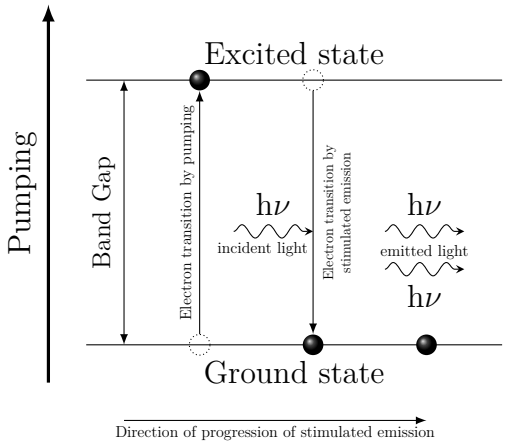

Figure 2.1 *Illustration of basic stimulated emission mechanisms.*

ture employs a resonant cavity which traps the emitted photons until their density is high enough [6, p. 5]. After the photon density surpasses the critical level of lasing threshold, the photons escaping the cavity are more from the stimulated than from the spontaneous emission. Beyond the lasing threshold most of the pumping energy is transferred into stimulated emission.

2.2 Distributed Feedback Edge Emitting Lasers

In a distributed feedback (DFB) (edge emitting laser (EEL)), the gain material and cavity feedback are distributed along the length of the device (see Figure 2.2 for different types of feedback). While the transverse structure ensures single transverse mode operation, the DFB EEL uses gratings to achieve selective feedback for just one longitudinal mode within the gain spectrum of the active material. These gratings are essentially a longitudinal variation of the effective refractive index that the electromagnetic wave experiences travelling along the structure. The device characteristics can be largely engineered by choosing the type and parameters of the gratings.

2.2.1 Mode Degeneracy

A problem encountered when a homogeneous grating and perfectly anti-reflection (AR) coated end facets are used in a DFB is the inherent mode degeneracy. Two modes on both sides of the stop band of the grating, closest to the Bragg wavelength [10], have identical mirror losses [11]. Depending on the gain spectrum of the active material, the two modes reach lasing threshold almost simultaneously. Several methods have been developed to eliminate this modal degeneracy and obtain

single longitudinal mode (SLM) operation. Most common are: (distributed) phase shifts (DPSs) and asymmetric facet mirrors.

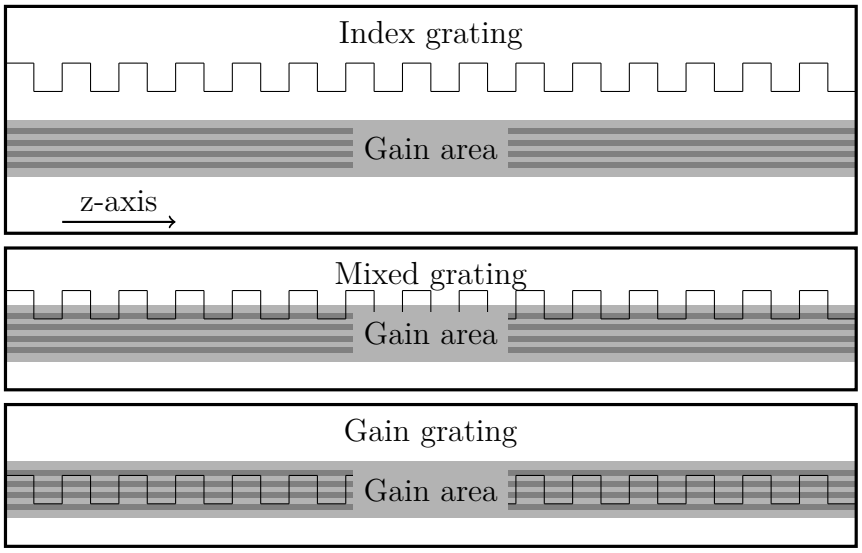

Figure 2.2 *Different types of gain and gratings in quantum well DFB lasers. The gain is from the layered area.*

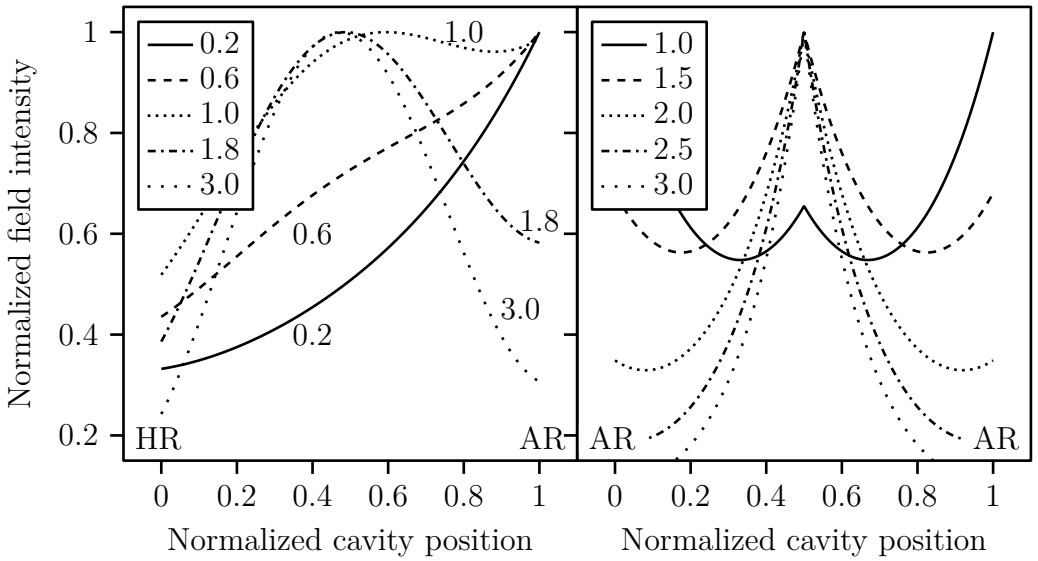

Figure 2.3 *Longitudinal envelopes of optical field distributions for two types of SLM lasers with varying grating coupling strengths. Left panel is HR-AR (95 % - 2%) coated DFB without any phase shifts. The left side is the HR facet. Right panel is an AR-AR (2 % - 2%) coated DFB with a $\pi/2$ phase shift in the middle of the cavity. The grating coupling strengths are given in the legends.*

Introducing a $\pi/2$ phase-shift (PS) in the otherwise periodical grating leads to one mode having the lowest mirror losses, at a position corresponding to the Bragg wavelength within the stop band of a homogeneous grating. This approach reduces

the strength of the spatial hole burning (SHB), but SHB remains an issue [12]. The longitudinal optical field distribution is concentrated mostly around the PS. The magnitude of this field concentration depends on the grating coupling strength, κL, where κ is the grating coupling coefficient and L is the total grating length. The field distribution for such a structure is illustrated in the right panel of Figure 2.3. Since the gain saturates in the regions with high field intensity, increasing the pumping beyond the saturation threshold in the high intensity regions contributes to the competing longitudinal modes with different field distribution inside the cavity, reducing the side mode suppression ratio (SMSR) and eventually leading to unwanted multi-longitudinal mode lasing.

Various combinations of end facet reflectivities (in terms of magnitude and phase) are also used to mitigate the longitudinal mode degeneracy. The most common approach is to employ high-reflection (HR) and anti-reflection (AR) coatings on cleaved facets, whose phase with respect to the gratings cannot be controlled. However, since the HR-AR facet coating also promotes high variation in the optical field intensity along the cavity (as illustrated in the left panel of Figure 2.3), the effects of SHB and the possibility of catastrophic optical damage (COD) [13] become significant. Since with a HR-AR facet coating the field intensity is highest at the AR-coated facet (albeit only up to a certain coupling strength level), COD is very likely to occur, particularly when carriers flow next to the AR-coated facet. COD near the facet causes irreversible damage to it.

Another way to circumvent the longitudinal mode degeneracy while avoiding SHB is to distribute the $\pi/2$ PS in several sections (i.e. DPS), so that the longitudinal distribution of the field intensity inside the cavity is flattened. The flatness (F) of the longitudinal field distribution is a figure of merit for SHB and can be evaluated by:

$$F = 1/L \int_{\text{cavity}} [I(z) - I_{\text{avg}}]^2 \, dz, \tag{2.1}$$

where L is the length of the laser cavity, $I(z)$ is the optical field intensity at point z in the cavity, and I_{avg} is the average field intensity in the cavity. When F is minimized, the optical field envelope is flat, and the effect of SHB is also minimized. This also means that the κL product can be higher without compromising the SLM operation. With increased κ, L, or κL, many laser characteristics, such as spectral linewidth $\Delta\nu$ are improved [14, 15]. However, complicated DPS structures are difficult to manufacture precisely and the gain margin of the main mode to the side modes is reduced.

2.3 Dual Wavelength Lasers

Lasers emitting at two wavelengths enable new kinds of approaches when it comes to applications such as differential sensing, coherent optical communications, and DFG for different frequency ranges, such as terahertz (THz), or extremely high frequency (EHF), often called millimetre wave (MMW) due to the wavelength being between one and ten millimetres. The main ways that are used to achieve dual wavelength emission are discussed in this section together with their advantages, disadvantages, as well as their current and potential applications.

2.3.1 Approaches for Achieving Dual Wavelength Emission

The obvious straightforward way to achieve dual wavelength emission is to use two separate lasers. Although flexible in terms of adjusting the powers and emission wavelengths of the two lasers independently, this approach has several disadvantages. These include system complexity, joint coupling difficulties, uncorrelated phase and noise, complex control, and different linewidths. The problems arise mostly from the lack of correlation and coherence between the two lasers. The presence of these attributes are, however, vital for many applications.

Several different approaches have been used to generate correlated and coherent dual wavelength emission. There has been some success in using two different transverse modes of the laser cavity [16]. However, although emitted from the same cavity, the two different transverse modes have a limited correlation due to the fact that they are distributed differently on the transverse cross section of the laser device and interact only in the area where they overlap. This reduces the efficiency of dual mode interaction and mode correlation considerably. Moreover, the frequency spacing of the two transverse modes cannot be controlled effectively and it is limited by the small effective refractive index difference between the modes.

A better approach in terms of controlling the frequency difference between the two emitted modes is to use two gratings with different Bragg wavelengths [17]. If both these gratings interact properly with the optical field and the mode competition allows dual wavelength emission, this approach gives greater flexibility in choosing the two wavelengths and their spacing. Usually the two different gratings are placed laterally along the sides of the laser cavity. This results in a situation where the two modes distribute transversely in such a way as to have a negligible interaction with each other's resonant gratings. Unfortunately, this situation also leads to reduced mode interaction and correlation.

A popular way to implement dual wavelength operation is to use an injection locked laser setup where there is no locking. In a typical injection locked setup there are two lasers, one is a stable single-frequency low-noise master laser whose emission is coupled into a second, high-power slave laser. When the injection is strong enough and the self-resonant frequencies of the two lasers are close enough to each other, the slave laser is locked by the injected field to the frequency of the master. The maximum frequency offset over which the locking is possible increases with the level of injection. Injection locking is generally used when a high output power needs to be combined with a very low intensity and phase noise. However, when the injection is not strong enough, the master laser frequency only shifts the slave lasers frequency toward its own. This phenomenon is known as frequency pulling. Under these conditions the system emits at two distinct wavelengths and there is more flexibility in controlling the two wavelengths and their spacing. Unfortunately reduced injection also means reduced mode interaction and correlation. Moreover, an injection locking setup is a complex system, comprising of components such as two lasers, couplers, and isolators. All the drawbacks from the complexity, including alignment difficulties, limited stability, difficult and expensive fabrication, increased footprint, and increased power consumption, make the injection locking setup difficult to operate in applications where a compact solution would be preferable.

The approach used in this thesis is to obtain dual wavelength emission from monolithic laser structures employing multiple longitudinal sections. These lasers operate in a dual longitudinal mode self-injection scheme. Having two longitudinal modes with different wavelengths but the same transverse profile alleviates the problem of mode interaction. The transverse mode overlapping given by:

$$\eta = \frac{\left|\int E_1(x,y)^* E_2(x,y)\right|^2}{\int |E_1(x,y)|^2 \int |E_2(x,y)|^2}, \tag{2.2}$$

where $E_i(x,y)$s ($i \in \{1,2\}$) are the transverse mode profiles, is an important factor in achieving mode interaction and correlation. In the case of two longitudinal modes with nearly identical transverse mode profiles the transverse mode overlap approaches unity. This increases the transverse mode interaction substantially, while the phase matching achieved by the multiple longitudinal sections ensures significant longitudinal mode interaction (see for illustration the constructive interaction section from Figure 2.4). Multiple longitudinal sections also enable controlled mode competition and selective pumping for controlling both the mode spacing and power

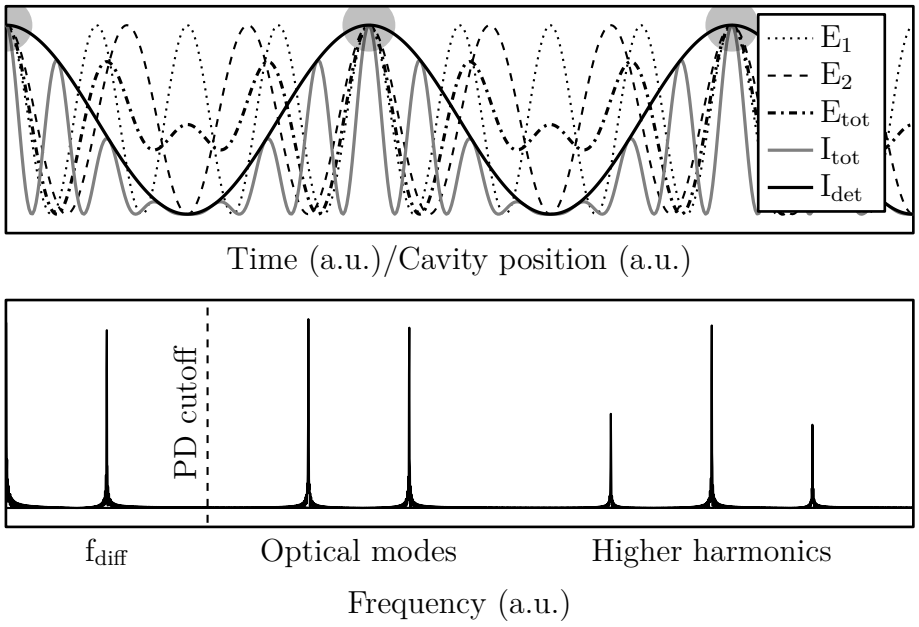

Figure 2.4 *Illustration of two modes with slightly different wavelength beating together at a fixed spatial location, and the FFT transforms of those signals. E_1 and E_2 are the optical mode amplitudes, E_{tot} and I_{tot} are the total amplitude and intensity, respectively, and I_{det} is the part of the intensity detected by the photodiode. Constructive interference maxima are highlighted with red circles, and all the lines are normalized to the same interval. The lines are color coded the same in both parts. Photodiode cutoff frequency is also shown in the FFT. Reciprocally the beating phenomenon is similar if the time is fixed and the position in the cavity is changing.*

balance. Figure 2.5 shows measured and simulated dual mode emission with relatively good mode power balance and mode spacing varied by laser structure design from 47 GHz to 1 THz. This freedom of choosing the coarse mode frequency difference is another advantage of this approach.

2.3.2 Difference Frequency Generation

Applying dual mode radiation to a photodiode (PD) [18, 19] with the cut-off frequency above the beating frequency of the two modes results in a photocurrent modulated with the beating frequency [20]. The difference-frequency is generated from the beating of the two modes with different frequencies in a similar manner as the beating of the two modes occurs at a given point in the laser cavity as illustrated in Figure 2.4. Taking into account that for high-speed PDs, similar to those used in the experiments described in this thesis, the absorbing layers are thin, the

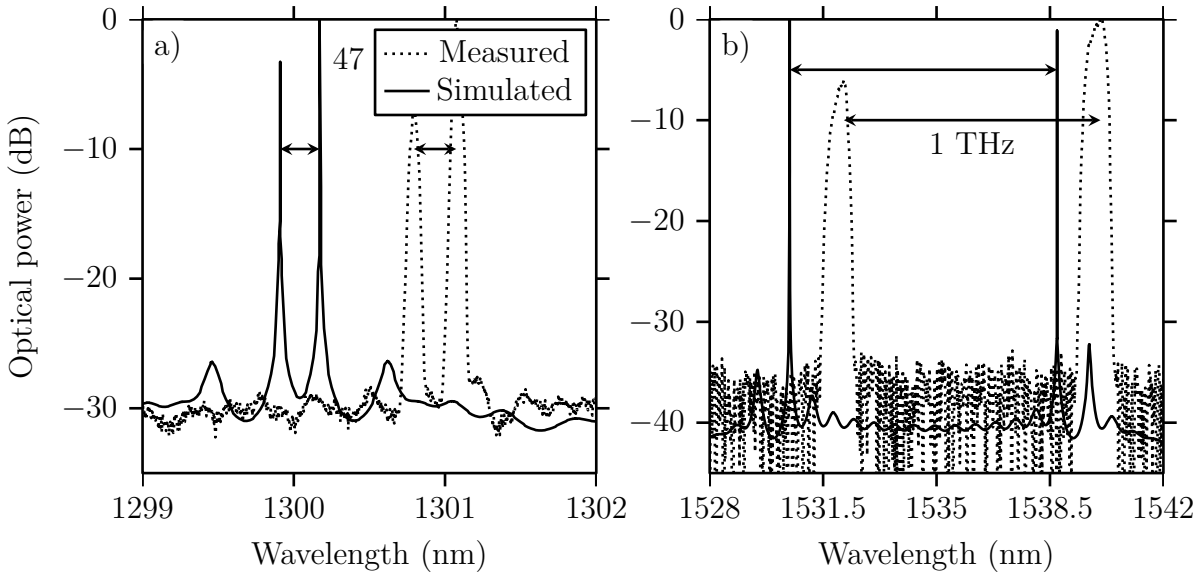

Figure 2.5 *Measured (·····) and simulated (——) spectra with a) 47 GHz mode spacing at 1300 nm central wavelength, and b) 1 THz mode spacing at 1535 nm central wavelength.*

total optical field intensity generated by the two modes can be approximated by the following simplified analytical expression:

$$\begin{aligned} I_{\text{tot}} &= |\mathbf{E}_{\text{tot}}|^2 = \sqrt{\Re\{\mathbf{E}_{\text{tot}}\}^2}^2 = \Re\{e^{-j\omega_1 t} + e^{-j\omega_2 t}\}^2 \\ &= \cos^2\omega_1 t + \cos^2\omega_2 t + 2\cos\omega_1 t \cos\omega_2 t \\ &= 1 + \cos(2\omega_1 t)/2 + \cos(2\omega_2 t)/2 + \cos(\Delta\omega t) + \cos((\omega_1+\omega_2)t), \end{aligned} \tag{2.3}$$

where E_{tot} is the total field, ω_1 and ω_2 are the two different angular frequencies and $\Delta\omega$ is their difference. Equation (2.3) uses basic trigonometric identities, and omits the spatial distribution of the optical field inside the PD and thus is only valid at a given penetration depth for a transversely uniform optical field. It also assumes unit amplitude for both waves. Because the existing PDs cannot follow the optical frequencies the optical field intensity experienced in the thin absorbing layer of the PD can be further approximated by:

$$I \sim 1 + \cos(\Delta\omega t). \tag{2.4}$$

It should be noted that the approximation given by Equation (2.4) is not accurate for all PD structures. Depending on the application, a PD may be designed in various configurations, e.g. waveguide integrated pin PD [21], travelling wave (TW) PD [22] or unitraveling-carrier PD [23]. The mode beating signal detected by the PD can be used for several applications, such as signal processing, wireless transmission or as a THz source.

2.3.3 Radio-over-Fiber

Radio over fiber (RoF) is a promising application for dual wavelength laser sources. The technique is used to reduce the total network complexity and cost. Figure 2.6 [24] gives a schematic overview of a typical RoF network. Because the signal is delivered optically to the base stations, no expensive electrical amplification components are needed there. For higher modulation rates the radio carrier frequency has to be higher. The downside with these high frequency radio transmissions, such as 60 GHz for the wirelessHD standard [25] or higher frequencies, is that the atmospheric absorption is relatively high, and transmission distances are limited to a few meters [26]. However, high attenuation means that the signals are inherently secure, and can be directed for only the audience within a small cell. Furthermore many of these frequency bands are unlicensed and due to that RoF is simple and cost-effective to implement.

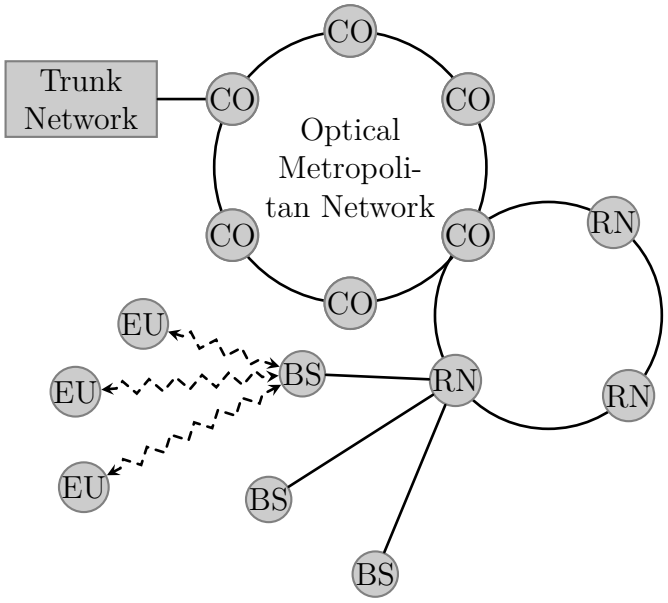

Figure 2.6 *A sketch of a typical RoF network. In the central offices (CO) the needed signal is extracted from the trunk network, and converted to RoF optical signal. This signal is then forwarded by optical fibers to the base stations (BS), possibly via remote nodes (RN). At BSs the optical RoF signal is converted to an electrical one and sent to the end users (EU). BSs are (usually) bidirectional such that EUs can also send information upstream. After [24].*

Dual mode lasers are ideal for carrying these high frequency signals optically over long distances up to a point where a set of radio transmitters can be used to cover

each a limited area, e.g. a multi storey building, for wireless transmission. Before the radio transmission a PD is used for DFG, and the resulting signal is then sent to an antenna from where it eventually goes to the end user device antennae.

In RoF the high frequency signal is encoded into the laser signal. Due to chromatic dispersion, using external modulators and direct detection to encode high frequency RF signal into a single optical carrier causes severe power penalty to the modulated signal inside an optical fiber [27, 28]. This power penalty is reduced by using a dual mode laser for remote heterodyne detection, but the transmission distances are still limited [27, 28]. In remote heterodyne detection one great advantage is that the LO is sent with the modulated signal, which reduces needed base station (BS) electrical components and complexity [24, 29]. This also reduces the modulation component requirements, because up/down-conversion is not needed at any stage and the laser modulation has to be only at the symbol rate.

At present there are already some implementations and experiences of RoF. The implementations usually fix problems with either very high capacity or very poor wireless connectivity [30]. These large and adaptable systems are complex in nature and require great multi-layer engineering effort in order to fit the changes induced by the optics into the already challenging radio transmission system working at the distortion limit [31].

2.3.4 Terahertz Radiation by Difference Frequency Generation

THz is a promising application for the new device designs. Dual mode lasers with difference frequency in the terahertz range have been fabricated and reported ([32] and Figure 2.5).

THz is an important area of research for several reasons. Because of its strong interaction with different phases of matter, THz can be used in many scientific fields such as spectroscopy, and even manufacturing processes, for example in machining [33]. Because of the high frequency, it has also been used in high speed wireless communication links [34]. However, because of high atmospheric absorption [35], the range of the data transmission is limited. The radiation penetrates many every-day materials more than normal light. This enables THz to be used as a security measure for example at airport terminals [36], where having a reliable, fast and safe way to assess whether a person is carrying forbidden items has become increasingly important in the political atmosphere of today [37]. Another useful application is in medical imaging [38]. The use of low energy THz gives the ability to get tomography images from human tissues with few harmful effects [39].

2.3.5 Modulation and Modulation Response

One main goal in data transmission is to bring down the cost per bit. To achieve this, cheap, compact and mass-producible sources are needed. To imprint the data to the transmitted signal, the output of the laser is modulated. In direct small signal amplitude modulation a small signal at the modulation frequency is put on top of the bias current, which is above the lasing threshold [40]. Small signal means that the modulation signal keeps the bias well above the lasing threshold. If the modulation response is relatively flat up to the maximum modulation frequency, the modulation transforms the electrical information into optical domain with precision [41] and optical data transmission is possible.

There are two categories of modulation response: amplitude and frequency. The conventional amplitude modulation (AM) response means that the modulation signal is transferred into amplitude variation of the laser output. After transmission this signal can be extracted by detecting the optical beam with a PD and measuring the variation of the electrical signal intensity. The bandwidth of the laser response to AM is limited by carrier-photon resonance (CPR) frequency. After this limit the photon and charge carrier population in the laser cannot follow the input current variation, and the response dies off.

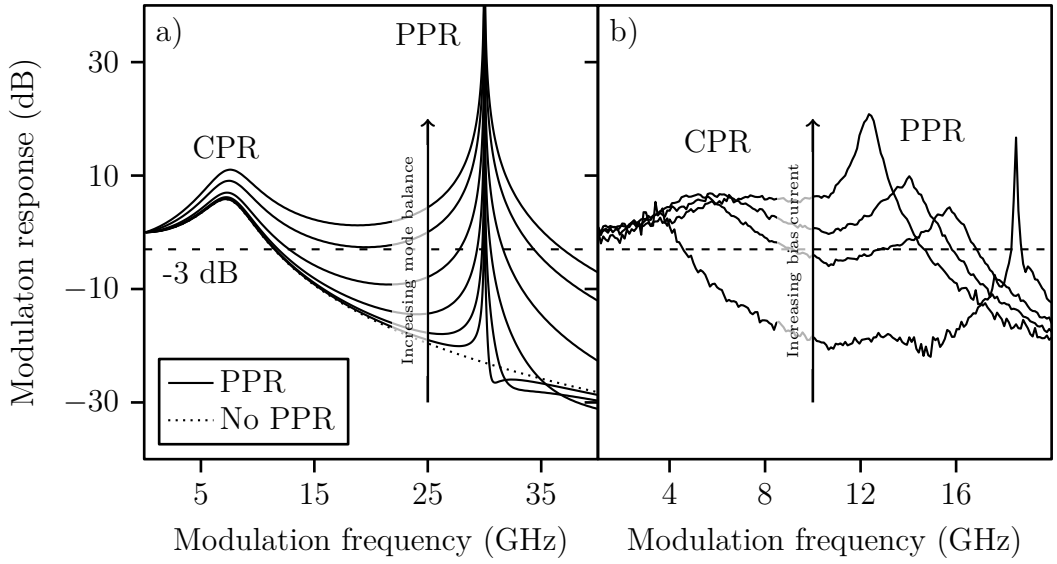

Figure 2.7 *a) Simulated modulation response with and without PPR in the model, with varying dual mode balance. b) Measured modulation response of a dual-mode laser with changing bias current.*

With conventional SLM lasers the CPR sets a limit on the modulation bandwidth. This limit can be countered by employing two-mode lasers. The modulation bandwidth is significantly greater, due to photon-photon resonance (PPR) between the

two modes [42]. PPR is the beating of the two modes, and the frequency of the beating is exactly the difference frequency of the two modes. Using the extended rate equations [42], where the longitudinal confinement factor is also considered as a dynamic variable, the modulation transfer function can be derived for dual mode lasers. The results shown in Figure 2.7 illustrate that the amplitude of the modulation response of a dual mode laser has an extra peak at the difference frequency of the two modes. By placing the PPR peak properly with respect to the CPR peak, and by adjusting it so that the modulation response is relatively flat, the AM modulation bandwidth can be extended. This technique can be used to exploit two-mode lasers for high frequency amplitude modulation.

For the dual mode lasers the frequency modulation (FM) response is also interesting. FM response means there is a change in the difference frequency of the laser due to small signal direct modulation. Whereas with conventional AM response (see Figure 2.7) there is an amplitude response, with FM the change is in the difference frequency as a function of the modulation signal. A $H(\nu) = \Delta\nu$ modulation transfer function (similar with Figure 2.7 but with $\Delta\nu$ as the vertical axis) shows how fast the difference frequency of the lasers can be tuned.

2.3.6 Mode Competition

Normally, when considering SLM lasers, mode competition becomes an issue between the lasing mode and competing modes. Through SHB the other longitudinal modes get gain from different spatial locations in the gain medium than the main mode, and they may also start lasing [43]. SHB then leads to a decrease in the competition for gain between different modes [44]. In a dual-wavelength laser the goal is to have two modes, and in a monolithic semiconductor laser the lasing modes share the gain at least partially. This means that when the power of one mode increases, the power of the other must decrease [43]. The phenomenon is sometimes called the gain lever (GL) [45]. The mode competition usually has an adverse effect on the mode balance and stability [44]. Physically the basis for mode competition lies in the gain material conduction-band intraband relaxation. The relaxation couples the modes that partially share the carrier population [46]. The intraband relaxation time for usual semiconductors is approximately 100–200 fs, and this leads to coupling-limiting upper frequency difference of 460–920 GHz [46, 47]. This means that if the mode spacing is less than this limit, there is strong coupling between them through various carrier scattering processes [48].

To get insight into the coupling between the two modes, a dimensionless coupling

parameter can be used [43]:

$$C = \frac{\theta_{12}\theta_{21}}{\beta_1\beta_2}, \tag{2.5}$$

where θ_{jk} is the cross-saturation coefficient and β_n is the self-saturation coefficient. A general expression for a cross-saturation coefficient is

$$\theta_{jk} = \frac{\mu^2\omega_0\tau_{in}(\tau_c+\tau_\nu)}{2\epsilon_0\hbar n n_g}\frac{g_L(\omega_k)}{g_L(\omega_0)}\frac{C_{jk}}{(1+\delta_{jk})C_k}\cdot\left(1+\frac{1+\alpha_k\Omega_{jk}\tau_c}{1+{\Omega_{jk}}^2{\tau_c}^2}\right), \tag{2.6}$$

where Ω_{jk} is the mode separation and C_{jk} is the overlap factor between modes j and k. For a self-saturation coefficient ($\beta_j = \theta_{jj}$) the two last terms become 0.5 and 2, respectively, and cancel each other. The rest of the details are given in [49]. Depending on the mode separation, both spectral and spatial within the active volume of the laser, as well as the location of the modes with respect to the gain maximum [49], the θ_{jk} terms can dominate the self saturation. Stable dual-wavelength lasing requires, however, that C < 1 [46], that is the product of the self-saturations of the mode pair is greater than the cross saturation. This condition also implies that the SLM operation domain is not stable [50]. The cross saturation is reduced when the two modes are spatially separated. This can be done for instance by separating the two modes in an external cavity [51, 52]. The issue with this approach is the complexity and thermal tuning, which gives a theoretical upper limit for tuning speed or frequency. The limit is given by the thermal time constant but in practice precise temperature control is not as fast as the time constant implies due to overshoot and oscillations. Thermal tuning can also be used in monolithic designs to achieve good tunability [53], but again the tuning speed becomes an issue.

For the design in this thesis the spatial separation is achieved through the separation between the longitudinal field profiles or the standing wave patterns. This also indicates that the SHB effect is essential for the design. Modulation induces changes in the field distributions which leads to changes in the mode balance. This is an issue for all electrically modulated dual-mode semiconductor lasers [53], especially if the modulation depth is large.

Longitudinal field distribution asymmetry induces an additional mode power imbalance problem: the mode whose field is concentrated farther from the lasing facet undergoes more losses before exiting from the lasing facet. This could be compensated for example by using asymmetric facet coatings (HR coating at the non-lasing facet) to boost the power of the farther mode [53]. Another option is to stabilize the mode balance with a feedback from the mode imbalance [44].

Loss variations also influence the balance between the two modes. In addition to the electrical field variation in modulation, the balance is affected by temperature, cavity defects or processing inaccuracies, changes in cavity length through mechanical vibrations, or other environment dependent variables [43, 44]. Stable dual-mode lasing then requires minimizing the sensitivity of the two modes to loss variations.

To model the mode balance problem above threshold, both the carrier distribution and mode field intensity distributions should be calculated [43, 44]. However, in this work the analysis is limited to the threshold and the optical field distribution analyses. In reality, the manufacturing accuracy of the devices induces greater variation in device performance than simulation inaccuracies, regardless of whether above threshold or threshold analyses are used.

A convenient concept when dealing with dual-mode lasing is the two-color point [46]. At this operating point the power balance shifts from one mode to the other. For the devices in this work the sign of the change in the difference frequency also changes (see Figure 5.1 b) for an example).

2.4 Transfer Matrix Method

The transfer matrix method (TMM) is a convenient way to represent complex multilayer structures as a series of simple structures. There are multiple ways to formulate the model: in this section the fundamental and the coupled wave methods are introduced. The fundamental method breaks the structure into its smallest homogeneous pieces, and models each piece and interface with a matrix. Coupled wave based formulation describes a section with constant structural parameters, such as coupling coefficient and effective refractive index, with a matrix.

2.4.1 Fundamental TMM

Fundamental TMM is based on the well-known theory of reflection, transmission and propagation of light. Although the effect was first studied by Ibn Sahl [54], the transmission and reflection coefficients are named after Fresnel, whose appropriate works are collected in for instance [55]. The coefficients for TE (s or $\perp$) and TM (p

or ∥) -polarized light are

$$t_{12}^{\mathrm{TE}} = \frac{2n_1 \cos\theta_i}{n_1 \cos\theta_i + n_2 \cos\theta_t} \tag{2.7}$$

$$r_{12}^{\mathrm{TE}} = \frac{n_1 \cos\theta_i - n_2 \cos\theta_t}{n_1 \cos\theta_i + n_2 \cos\theta_t} \tag{2.8}$$

$$t_{12}^{\mathrm{TM}} = \frac{2n_1 \cos\theta_i}{n_1 \cos\theta_t + n_2 \cos\theta_i} \tag{2.9}$$

$$r_{12}^{\mathrm{TM}} = \frac{n_2 \cos\theta_i - n_1 \cos\theta_t}{n_1 \cos\theta_t + n_2 \cos\theta_i}, \tag{2.10}$$

where θ_i is the incident angle, θ_t is the transmission angle, n_1 and n_2 are the refractive indices on the incident and transmitted side of the interface, respectively (illustrated in Figure 2.8), superscripts TE and TM refer to the polarization, subscript 12 refer to the direction of reflection and transmission (from material 1 to material 2), and t_{it}^x and r_{it}^x are the amplitude transmission and reflection coefficients, respectively. Incident and transmission angles are related according to the law of refraction (see for example [56, p. 101]) (commonly known as Snell's law)

$$\frac{\sin\theta_i}{\sin\theta_t} = \frac{n_2}{n_1}. \tag{2.11}$$

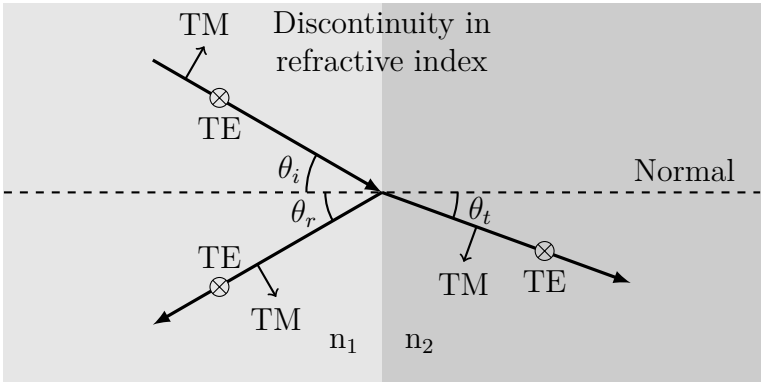

Figure 2.8 *Interface between two media with different refractive indices.*

When considering a 1-D situation, the propagation of a plane wave in a homogeneous medium can be expressed by

$$E(x,y,z,t) = E_0(x,y)\exp(-i\beta z)\exp(i\omega t), \tag{2.12}$$

from which the static z evolution results as

$$E(z+dz) = E_0(z)\exp(-i\beta dz), \tag{2.13}$$

where E is the amplitude of the wave, z is the position on the axis of propagation, $i = \sqrt{-1}$ is the imaginary number and $\beta = k + i\alpha/2 = 2\pi n_{\text{eff}}/\lambda + i\alpha/2$ is the complex propagation constant, where k is the wave number, λ is the wavelength, n_{eff} is the effective refractive index and α is the net absorption (or gain) coefficient.

However, in a multilayer case, there are always both forward and backward propagating waves. For this reason the field at a position z must be a superposition:

$$E(z) = E^{+}\exp(-i\beta z) + E^{-}\exp(i\beta z), \tag{2.14}$$

where the superscripts $^{-}$ and $^{+}$ refer to forward and backward propagation, respectively. Such a superposition of waves at the beginning and end of a uniform medium can be written using matrix notation as [57]

$$\begin{bmatrix} E^{+}_{\text{end}} \\ E^{-}_{\text{end}} \end{bmatrix} = \begin{bmatrix} \exp(-i\beta dz) & 0 \\ 0 & \exp(i\beta dz) \end{bmatrix} \begin{bmatrix} E^{+}_{\text{start}} \\ E^{-}_{\text{start}} \end{bmatrix}, \tag{2.15}$$

where subscripts $^{\text{start}}$ and $^{\text{end}}$ refer to the beginning and end interfaces of the uniform section of propagation medium.

If the medium where the waves are propagating is active, the imaginary part of the propagation constant includes optical gain and losses [11]. With the notation from Equation (2.13) the complex propagation constant expands to

$$\beta = \beta_r + i\beta_i = 2\pi n_{\text{eff}}/\lambda + i\frac{g - \alpha_{\text{int}}}{2}, \tag{2.16}$$

where g is the optical gain, α_{int} is the internal loss, and subscripts r and i refer to real and imaginary parts. Similarly, a complex effective refractive index is defined by including an absorption part [11]

$$\tilde{n} = n + \frac{i\alpha\lambda}{4\pi}, \tag{2.17}$$

and applying it to the Fresnel coefficients in Equations (2.7) to (2.10).

The propagation matrix in Equation (2.15) is usually denoted by $\mathbf{T}$, and thus the Equation (2.13) can simply be written as

$$E(z + dz) = \mathbf{T}E(z), \tag{2.18}$$

with the electric fields considered as vectors with forward and backward propagating components.

Similarly such a matrix notation can be used for interfaces of two media where reflection and transmission occur. The matrix uses Fresnel coefficient from Equations (2.7) to (2.10), and can be written as

$$\mathbf{R} = \begin{bmatrix} 1/t_{21} & -r_{12}/t_{21} \\ -r_{12}/t_{21} & 1/t_{21} \end{bmatrix}. \tag{2.19}$$

A product of **T** and **R** matrices describes the total effect of a 1D-structure. The product matrix is usually denoted by **M**:

$$\mathbf{M} = \begin{bmatrix} m_{11} & m_{12} \\ m_{21} & m_{22} \end{bmatrix} = \mathbf{R}_i\mathbf{T}_i\mathbf{R}_{i-1}\mathbf{T}_{i-1}\cdots\mathbf{T}_2\mathbf{R}_1\mathbf{T}_1\mathbf{R}_0, \tag{2.20}$$

where each matrix $\mathbf{T}_j$ and $\mathbf{R}_j$ describe transmission and reflection, respectively. Indexing of the matrices starts from the side of the entering wave, and reads backwards. With this approach it is possible to model any kind of longitudinal laser structure. The only requirement is that the structure consists of homogeneous sections with a well defined plane of reflection in-between them. The construction of the total M matrix is shown schematically in Figure 2.9.

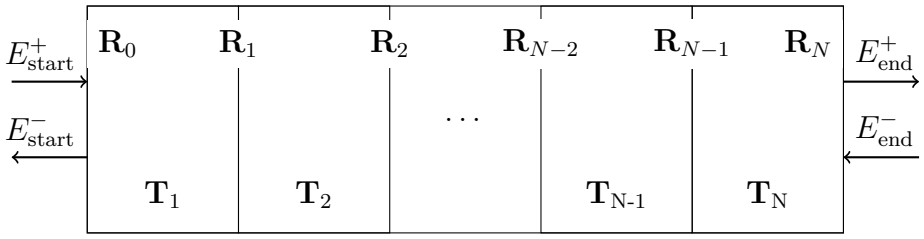

Figure 2.9 *A schematic illustration of the construction of an* **M** *matrix.*

The **M** matrix gives the total reflection and transmission coefficients of the structure when it is a passive device (no emission inside the structure). Setting unitary input from left facet, the relation between total coefficients and transfer matrix elements can be written as

$$\begin{bmatrix} T \\ 0 \end{bmatrix} = \begin{bmatrix} m_{11} & m_{12} \\ m_{21} & m_{22} \end{bmatrix} \begin{bmatrix} 1 \\ R \end{bmatrix}, \tag{2.21}$$

and the transmission and reflection coefficients as

$$T = m_{11} - \frac{m_{12}m_{21}}{m_{22}}, \tag{2.22}$$

$$R = -\frac{m_{21}}{m_{22}}. \tag{2.23}$$

Until now the analysis has been limited to passive devices. To model a laser emitter, active materials are included in the model. The complex propagation constant is used for this task. The imaginary part of the propagation constant is related to gain (and losses) inside the device. This way it is possible to have output from the device without any optical input.

To determine the lasing threshold the losses of one cavity round trip are first determined. The losses consist of α_{int} for each uniform section [11], and mirror losses α_{m}, which depend on the wavelength. If the overall gain from the structure is the same as the losses for the round trip, the gain condition is satisfied. This is still not enough because there has to be constructive interference between the forward and backward propagating waves. The wavelengths for which the total change in phase after a round-trip is a multiple of 2π satisfy the phase condition.

The laser is at lasing threshold at wavelengths where both the gain condition and the phase condition are satisfied. It is important to note that this model takes into account only the balance between the gain, mirror and internal losses, and the phase condition. However, several other mechanisms, such as temperature, dispersion and gain saturation affect the laser behaviour [58, 59]. These mechanisms are beyond the scope of this thesis.

Effective Index Tuning

An approximate modelling of the effects from different laser diode usage scenarios, such as non-uniform pump current, temperature gradients and carrier concentration variations, can be based on effective index variation. Each of these situations is associated with an effect on the refractive index of semiconductors, and consequently, on the effective refractive index experienced by the electromagnetic waves inside the laser cavity. The magnitude of the index variation can be approximated theoretically or from experimental results [60, 61].

These effects are included in the model by changing the effective index in parts of the laser by a factor ξ, and the *tuned* effective index of a laser section becomes

$$n_{\text{eff}}^{\text{tun}} = \xi n_{\text{eff}}. \tag{2.24}$$

In a uniform bias condition without asymmetries the factor ξ has a value of 1 everywhere in the cavity.

2.4.2 Coupled Wave TMM

Another way to formulate the transfer matrices is through the coupled wave theory [62]. The difference in comparison to the fundamental TMM is that each section of the laser which has constant structural parameters is considered an individual block, and the formulation does not go to the individual sections as in the TMM formulation of the previous section.

The propagation of an electromagnetic wave is described by the wave equation [63]

$$\nabla^2\mathbf{E} + k_0^2 n^2 \mathbf{E} = 0, \tag{2.25}$$

where n is the refractive index, k_0 is the propagation constant in vacuum and $\mathbf{E}$ is a time harmonic with the angular frequency ω. This assumes that the media of propagation is constant.

For a DFB laser the equation reduces to a spatially 1-dimensional case due to the assumed confinement of the electromagnetic field in the transverse plane. Further, a DFB is not longitudinally homogeneous, and some mechanism must describe perturbations. The coupling coefficient combines perturbations in refractive index (real part) and gain (imaginary part) and expands to [62]

$$\kappa = \kappa_i + j\kappa_g, \tag{2.26}$$

where indices i and g depict index and gain, respectively. For the case of purely index coupled rectangular lattice the coupling coefficient is [64]

$$\kappa = \frac{k_0}{2n_{\text{eff}}}(n_{\text{eff2}}^2 - n_{\text{eff1}}^2)\frac{\sin(\pi m\gamma)}{\pi m}, \tag{2.27}$$

where n_{eff2} and n_{eff1} are the longitudinally alternating effective indices, m the grating order and γ is the filling factor. The *perturbed propagation constant* includes this perturbation in the wave equation:

$$k^2(z) \approx \beta^2 + 2j\beta\alpha_0 + 4\kappa\cos(2\beta_0 z + \Omega), \tag{2.28}$$

where $\beta = k_0 n_0$ (note the different notation compared to Section 2.4.1), α_0 is the unperturbed gain, n_0 is the unperturbed refractive index, β_0 is the Bragg propagation constant [10] and Ω is the non-zero residual corrugation phase at $z = 0$. The approximation comes from the fact that $\Delta n \ll n_0$ and $\Delta\alpha \ll \alpha_0$ [62]. This is one of the fundamental assumptions of the coupled wave theory.

Now the wave equation for a perturbed 1-D case becomes

$$\frac{d^2E}{dz^2} + \left[\beta^2 + 2j\beta\alpha_0 + 4\kappa\cos(2\beta_0 z + \Omega)\right] E = 0, \tag{2.29}$$

and expanding the cosine term into its exponential parts, one trial solution of the scalar equation is a combination of oppositely travelling waves. Acknowledging that the solution must be close to the Bragg frequency of the DFB grating, the trial solution can be written in terms of Bragg propagation constant and the detuning factor $\delta = \beta - \beta_0$ as

$$E_{\text{trial}}(z) = R(z)e^{-j\beta_0 z} + S(z)e^{j\beta_0 z}, \tag{2.30}$$

where R and S are the waves propagating in opposite directions. After inputting the trial solution into the wave equation (2.29), the equation can be separated into terms with common term $e^{-j\beta_0 z}$ and $e^{j\beta_0 z}$. Because of the coupled wave theory assumptions the fields are slowly varying, and the second derivatives vanish. Furthermore, since the operation point is near the Bragg frequency, the resulting high frequency terms, for instance $e^{3j\beta_0 z}$, can be neglected. The result is a pair of coupled wave equations:

$$S' + (\alpha_0 - j\delta)S = j\kappa R e^{j\Omega} \ , \tag{2.31}$$

$$-R' + (\alpha_0 - j\delta)R = j\kappa S e^{-j\Omega}, \tag{2.32}$$

where $'$ denotes the first order derivatives. The coupled waves R and S due to attenuation and amplification inside the laser cavity can be expanded as

$$S(z) = S_1 e^{\sigma z} + S_2 e^{-\sigma z}, \tag{2.33}$$

$$R(z) = R_1 e^{\sigma z} + R_2 e^{-\sigma z}, \tag{2.34}$$

where the attenuation or amplification constant σ arises from the boundary conditions. Comparing with Equation (2.32), it is clear that the parts R_1 and S_2 are amplified. By putting the expanded expressions for coupled waves into the pair of Equation (2.32), the similar terms can be collected again, resulting in [65]

$$\hat{\Gamma} R_1 = j\kappa e^{-j\Omega} S_1, \tag{2.35}$$

$$\hat{\Gamma} S_2 = j\kappa e^{j\Omega} R_2, \tag{2.36}$$

$$\Gamma S_1 = j\kappa e^{j\Omega} R_1, \tag{2.37}$$

$$\Gamma R_2 = j\kappa e^{-j\Omega} S_2, \tag{2.38}$$

with Γ and $\hat{\Gamma}$ shortening the notation

$$\hat{\Gamma} = \alpha - j\delta - \sigma, \tag{2.39}$$

$$\Gamma = \alpha - j\delta + \sigma. \tag{2.40}$$

The following relations further simplify the equations:

$$\frac{\hat{\Gamma}}{j\kappa} = \frac{j\kappa}{\Gamma} = \rho \tag{2.41}$$

and

$$\sigma^2 = (\alpha - j\delta)^2 + \kappa^2. \tag{2.42}$$

Now the coupled equations and end facet reflection coefficients are used to define the boundary conditions. From there it is possible to arrive at a transcendental function describing a DFB laser [65]. In reality, however, the structures are seldom this simple, and deriving equivalent equation for different structures is not sensible. Because of that a matrix notation can be derived, much like in Section 2.4.1, but now using the conventions used earlier in this section.

A laser cavity is separated into parts each having a set of parameters: effective refractive index, central wavelength, coupling coefficient and length. The formulation is more complex than with fundamental matrices. A derivation can be found for example in [66] and it is based on principles introduced earlier in this section. Construction of the total transfer matrix works much as in Section 2.4.1. The forward transfer matrices are used here: multiplying by the electric field at the left facet give the electric field at the right facet. The transfer matrix for one section with constant parameters is

$$\mathbf{T}(z_2|z_1) = \begin{bmatrix} t_{11} & t_{12} \\ t_{21} & t_{22} \end{bmatrix}, \tag{2.43}$$

where the elements are

$$t_{11} = \frac{(E_c - \rho^2 {E_c}^{-1}) \cdot \exp(-j\beta_0(z_2 - z_1))}{1 - \rho^2} \tag{2.44}$$

$$t_{12} = \frac{-\rho(E_c - {E_c}^{-1}) \cdot \exp(-j\Omega) \exp(-j\beta_0(z_2 + z_1))}{1 - \rho^2} \tag{2.45}$$

$$t_{21} = \frac{\rho(E_c - {E_c}^{-1}) \cdot \exp(j\Omega) \exp(j\beta_0(z_2 + z_1))}{1 - \rho^2} \tag{2.46}$$

$$t_{22} = \frac{-(\rho^2 E_c - {E_c}^{-1}) \cdot \exp(j\beta_0(z_2 - z_1))}{1 - \rho^2}, \tag{2.47}$$

where $E_c = \exp(\sigma(z_2 - z_1))$ and z_1 and z_2 are the start and end positions of the section, from left to right respectively.

A phase discontinuity along the laser cavity is an important element when designing and modelling a laser. To implement it in the current formulation, a phase shift matrix is introduced:

$$\mathbf{P} = \begin{bmatrix} e^{j\theta_k} & 0 \\ 0 & e^{-j\theta_k} \end{bmatrix}, \tag{2.48}$$

where θ_k is the amount the phase shift changes the phase of the wave and index k is the identifier of the phase shift.

Combining phase shift matrices (2.48) and corrugation matrices (2.43), a matrix describing the propagation of waves inside a cavity can be written as

$$\mathbf{Y}(z_N|z_1) = \prod_{n=N}^{1} \mathbf{T}_n \mathbf{P}_n, \tag{2.49}$$

where the $\mathbf{P}_1$ is an identity matrix for notational consistency.

Lastly, to model a realistic laser cavity, the end facet effects have to be included. As before, a new matrix is introduced and multiplied with the previous result (2.49). The reflection matrix is composed of both the amplitude reflection coefficient at the facet as well as the phase change the wave undergoes once it transverses the interface. The formulation is

$$\mathbf{R}_{\text{right}} = \frac{1}{e^{j\phi_2}\sqrt{1-r_2^2}} \cdot \begin{bmatrix} 1 & -r_2 \\ -r_2 & 1 \end{bmatrix} \text{ and} \tag{2.50}$$

$$\mathbf{R}_{\text{left}} = \frac{1}{e^{j\phi_1}\sqrt{1-r_1^2}} \cdot \begin{bmatrix} 1 & r_1 \\ r_1 & 1 \end{bmatrix}, \tag{2.51}$$

where ϕ_i is the phase change at facet passing and r_i is the amplitude reflectivity. The total forward propagating transfer matrix becomes

$$\mathbf{H} = \mathbf{R}_{\text{rigth}} \mathbf{Y}(z_N|z_1) \mathbf{R}_{\text{left}} = \begin{bmatrix} h_{11} & h_{12} \\ h_{21} & h_{22} \end{bmatrix}. \tag{2.52}$$

Using the notation from Equation (2.15) the lasing condition with the help of the coupled wave matrix $\mathbf{H}$ can be defined. A laser is such a device that without any optical input there is output when the device is lasing. If one of the incoming waves,

E^+_{start} is set to zero, the matrix equation simplifies to:

$$E^+_{\text{end}} = h_{12} E^-_{\text{start}} \tag{2.53}$$

$$E^-_{\text{end}} = h_{22} E^-_{\text{start}}. \tag{2.54}$$

The transmission gain coefficient for backward propagating wave becomes

$$A_t = \frac{E^-_{\text{start}}}{E^-_{\text{end}}} = \frac{1}{h_{22}}. \tag{2.55}$$

When matrix element h_{22} becomes zero, the transmission coefficient goes to infinity. At this point the device is lasing and by convention it is called *the lasing condition*. By scanning a wavelength range near the Bragg wavelength of the device the losses for each mode can be found, and the modes with lowest losses will be the ones most likely to lase. The minima of h_{22} can be found with multiple methods, such as the nonlinear Nelder–Mead optimization algorithm [67].

This method of matrix resonances also works for solving the lasing condition with the fundamental matrix approach. In fact, the method is more robust than the method of gain and phase condition searching used before: it finds the modes for even zero-reflectivity facet structures, which is impossible with the method introduced earlier.

Tuning in the Coupled Wave Formulation

The fact that in the coupled wave formulation each section of the laser is a separate block imposes some implementation problems when dealing with refractive index tuning. If the effective index is to be tuned, only changing the index by tuning amount ξ does not suffice. This is because the current formulation is matching the operating wavelength with other structural parameters. Changing only the effective index changes the grating period Λ in the structure to match the given central wavelength, which is not physically possible. A workaround to this problem is to give a definition for central wavelength through structural parameters.

The solution starts from the length of the device

$$L = \Lambda M = 2m \cdot \frac{\lambda_C}{4 \cdot n_{\text{eff}}} M, \tag{2.56}$$

where L is the physical length of the grating, Λ is the grating period, M is the number of mirror pairs or periods, m is the grating order, and λ_C is the center wavelength of the grating. The relation between the physical length of the device

and the number of mirror pairs, and the effective refractive index is determined. Now the change in the central wavelength due to tuning is evaluated from

$$\lambda_{\mathrm{C}} = \frac{2Ln_{\mathrm{eff}}}{mM} \cdot \xi. \tag{2.57}$$

From the above equation it is clear that the dependence of the central wavelength and tuning is linear. Using Equation (2.57), the change in the coupling coefficient under tuning is also determined. Assuming $m = 3$ and $\gamma = 0.5$ for simpler analysis, Equation (2.27) reduces to

$$\kappa = \frac{n_{\mathrm{eff2}}^2 - n_{\mathrm{eff1}}^2}{\lambda_{\mathrm{C}} n_{\mathrm{eff}} m}. \tag{2.58}$$

Using Equation (2.57) and also setting $n_{\mathrm{i}} = n_{\mathrm{i}}\xi$, κ becomes

$$\kappa = \frac{M\left[(n_{\mathrm{eff2}}\xi)^2 - (n_{\mathrm{eff1}}\xi)^2\right]}{2L(n_{\mathrm{eff}}\xi)^2}. \tag{2.59}$$

It is clear that the effective index tuning does not change the coupling coefficient. Leaving out the simplifications does not change the result. An important note is that the amount of effective index tuning does vary slightly between the two different effective refractive index values, n_{eff1} and n_{eff2}. The variation difference changes with for example filling factor and the composition of the laser structure. Because of this, κ has a slight dependence on the tuning index. However, this small amount can be left out, especially in the case when ξ is close to 1. In conclusion, to model refractive index tuning using the coupled wave approach, changing the effective refractive index and determining the change it imposes on the central wavelength are the only required steps in order to have a good enough approximation.

3. IMPLEMENTATION

This chapter discusses the software used in the thesis, the changes to it realized by the author and some example usage scenarios. Section 3.1 discusses the transfer matrix method software, its user interface and its usage in the design process. There are also example scripts for doing different kind of simulations. Section 3.2 introduces ways to use the software for design optimization.

3.1 Transfer Matrix Methods

The transfer matrix method software package combines three different algorithms. Fundamental version `fundamental` uses the basic TMM (Section 2.4.1) with the legacy solving algorithm [68]. The new version of the fundamental TMM `fundamentalNew` uses the matrix resonances based solving described in the end of Section 2.4.2. The coupled wave method version `coupled` uses the coupled wave formalism from Section 2.4.2.

The input gives a description of a longitudinal laser structure. With a value for the coupling coefficient, the average effective refractive index and the wavelength, the program can determine the effective refractive indices and mirror pair widths, the whole longitudinal structure. The user may also give the values for effective index and mirror pair widths explicitly. The list of these and other public properties for the class is in Table 3.1. Error checking notifies the user of mistakes in the input and possible problems during runtime.

The class supports instance arrays, and due to the embarrassingly parallel nature of these arrays they are calculated in parallel when possible (with MATLAB's `parfor` environment). To display the results interactively, the class overloads MATLAB's built-in functions `plot`, `contourf` and `pcolor`.

Program 3.1 *Script to run the TMM calculation with default parameters.*

```
L = LaserClass;    % Initiate the class instance.
L = L.calculate;   % Run the calculations.
L = L.evaluate;    % Post-process the results.
L.plot;            % Visualize the results in a plot.
```

The basic use scenarios of the class become evident through simple examples. In Listing 3.1 is a script to run the TMM calculations with default values. The user can inspect the properties by simply invoking `L`. It is straightforward to initiate a class instance array with default values. However, using specified properties in the array elements is usually more convenient. An example of this is in Listing 3.2.

Program 3.2 *Script to run the TMM calculation for an array. The value of property M is changing.*

```
% Initiate the seed instance.
L = LaserClass;
% Change static instance parameters here.
% Define array dimensions.
m = 8;n = 1;
% Define the range for the changing parameter(s).
Mvalues = round(linspace(150,250,m));
% Initiate the instance array.
LArray = LaserClass(m,n);
for i = 1:m
    % Change the instance property.
    L.M = Mvalues(i);
    % Save it in the array.
    LArray(i) = L;
end
% Run the calculations for the array
LArray = LArray.calculate;
% Output an ASCII table of properties
% and evaluated quantities.
LArray.printresults;
```

Using the instance arrays, or arrays of instance arrays, it is straightforward to generate complex multidimensional parameter sweeps and use the class for parameter optimization. Furthermore, because the memory requirements are relatively low per

simulation, the only limit for parallelization is the number of processor cores.

3.2 Optimization

In the design process of a laser, finding the set of structural parameters that achieve the best performance is crucial. However, defining laser performance is non-trivial, and almost always there are compromises between for example the linewidth and the dimensions of the laser. To find a set of maximized performance values, some principles from optimization are useful.

The simplest way to find the optimum design is to designate a feasible search space of structural parameters and calculate the performance values for each combination in this space. This ensures finding an optimum. However, such an approach becomes very time consuming when the calculation time of one instance is long and the number of parameters increases.

To tackle huge search spaces, several different algorithms have been developed [69, 70]. In this thesis the algorithm used is the particle swarm optimization (PSO) algorithm. It has been applied on several different search problems, and the results and convergence are illustrated later in Section 5.6.

In essence, the stochastic algorithms search for a minimum, so a suitable goal function is needed. If several variables are changing, one choice is a conventional weighted aggregate (CWA) [71]

$$\mathfrak{F} = \sum_{i=1}^{n} w_i f_i(\mathbf{x}), \tag{3.1}$$

where $\mathbf{x}$ is a k-dimensional vector of design parameters, f_i is a goal function, in our case a part of the performance value, and w_i is the weight associated with the corresponding f_i. The weights usually fulfill the condition $\sum w_i = 1$. This multiple in, single out (MISO) function is simple in terms of implementing different optimizers. However, the user cannot determine parts of the performance value separately, and they have to be weighed. This means that the user choices dictate largely how well this kind of optimization scheme works: the user can find only one pareto optimum per optimization run. It has also been shown that the CWA approach is unable to find the pareto optima on the concave pareto front or the concave regions of the pareto front [71, 72]. For this reason choosing the correct weights is important. Depending on which performance values are more important, the weights can differ significantly between optimization runs.

Sometimes it is convenient to be certain that the value of the CWA stays non-negative, so an addition to the Equation (3.1) can be made:

$$\mathfrak{F}_{\text{pos}} = \left[\sum_{i=1}^{n} \left(w_i f_i(\mathbf{x})\right)^m\right]^{1/m}, \tag{3.2}$$

where m is a positive integer. Now with real valued goal functions the CWA is always a non-negative number. Indeed, with $m = 2$ equation (3.2) resembles the l^2-norm. This may or may not be desirable, and the user has to decide depending on the task which type of CWA to use.

It is also possible to use evolutionary dynamic weighted aggregates, such as bang-bang weighted aggregate (BWA) or dynamic weighted aggregate (DWA) [71]. These methods can find the pareto front by changing the weight distribution either in steps (BWA) or gradually (DWA). The greatest benefit is that in principle these methods can find the pareto front without user interaction. Implementation, however, becomes problematic when the number of goal functions in the aggregate is large. In principle, to find the complete pareto front, the user should use all the combinations of the weights. Especially with computationally expensive aggregate functions this increases the simulation time considerably, and for the purposes of this thesis a well chosen CWA provides acceptable results in a reasonable time.

Table 3.1 *Public properties of a 1-D laser object for TMM simulations with descriptions.*

Property	Type	Description
`M`	array	Number of mirror pairs
`lambda`	array	Wavelength of the grating
`gamma`	array	Fill factor
`gammaType`	array	Fill factor type, physical or optical
`R1`	real number	Left facet power reflectivity
`R2`	real number	Right facet power reflectivity
`R1Phase`	real number	Left facet effect on phase
`R2Phase`	real number	Right facet effect on phase
`neff`	array	Effective refractive index
`kappa`	array	Coupling coefficient
`m`	array	Grating order
`detectionType`	string	Lasing mode determination in post processing
`detectionLambda`	array	Which wavelengths are used for lasing mode detection
`lambdaRange`	array	Wavelength span of the simulation
`resolution`	integer	Number of wavelength points
`w`	array	Length of the mirror pairs
`padding`	array	Extension between end of the grating and facet mirror
`simulationType`	string	Which simulation to run
`powerCalculation`	boolean	Determines whether power spectrum is calculated
`powerResolution`	integer	Cavity resolution in power calculation
`envelopeStep`	real number	Step length in the envelope evaluation
`envelopeLambda`	real number	Which wavelength the envelope evaluation uses (defaults to first lasing mode)
`envelopeAlpha`	real number	Which gain the envelope evaluation uses (defaults to first lasing mode)
`modulation`	array	Tuning amount ξ for coupled wave formulation
`material`	string	Layer structure name for dispersion implementation
`lengthRange`	array	Which lengths of the device the simulation runs
`P`	array	Number of phase shifts
`Ptype`	string array	The amount how much phase shifts affect the phase
`Plengths`	array	The lengths of the phase shifts for custom definition
`gain`	array	How much gain there is in each section (defaults to 1)
`ignoreBadOptBool`	boolean	Whether to stop if solver encounters bad values

4. MEASUREMENTS

This chapter describes the measurement setup and its development. The results from the measurements together with the simulation results are gathered in Chapter 5. A diagram of the measurement setup is presented in Figure 4.1.

4.1 Static Optical Characterization

In the first stage the performance of the available dual-mode chips by simple optical measurements was determined. The chips have multiple (2,3,...) contacts, which leads to n-dimensional bias-current maps. However, it was found that the chips performed well enough when only two of the bias currents are varied. This reduced the bias map dimension, and accelerated the characterization procedure considerably. However, the number of available chips for characterization required considerable efforts to determine good chips (with good dual-mode stability) and the correct bias ranges for these chips. Furthermore, slight variations in the contact resistances, and in the resistance between the probing station base and the chip resulted in the fact that the good bias values have variations of approximately 5 mA from measurement to measurement. This effect is only valid for the characterization of separate chips, and stable bias values for packaged devices are to be expected.

The laser drivers used were Thorlabs ITC 510 and LDC 240. The light from the chip facets was directed at a cleaved multi-mode fiber (MMF) and guided to an ANDO AQ6317C optical spectrum analyzer (OSA). The aluminum probing base had a stable temperature from a thermo-electic cooler (TEC) element driven by a Keithley 2510 TEC Sourcemeter.

4.2 Static Electrical Characterization

For the first electrical experiments a u^{2}t Photonics (at the time of the writing Finisar) PD XPDV2320R was used. The detector has a single-mode fiber (SMF) input and a collimator setup was used to get maximum coupling. To remove the spurious resonances between the collimator lenses an isolator was included in the setup

(Thorlabs IO-2.5-1310-VLP).

The highest bandwidth electric spectrum analyser (ESA) available was a 26.5 GHz Hewlett–Packard E4407B, so a mixer (Marki microwave M9-0943) had to be used to get the signal frequency down to the 26.5 GHz range. For the local oscillator (LO) a 30 GHz Rohde & Schwarz SMR30 was used. An electrical amplifier (Centellax UA0L65VM) was also used to boost the signal strength. The PD current from the coupled light was approximately 0.2-0.5 mA without optical amplification.

4.3 Low Frequency Analogue Modulation

For the initial modulation experiments an arbitrary pulse pattern generator (PPG) was used to modulate the laser drivers. The probe needles had a 3 dB cut-off frequency at 27 kHz. This limited the modulation frequencies to a few hundred kHz using the DC needles for modulation. Even though the modulation frequencies were low, the results showed the behavior of the chips under bias current modulation, and this indicated that higher frequencies were also worth investigating.

4.4 High Frequency Modulation

A high frequency (HF) probe from GGB Industries (customized model 40A, P-24-5503) was used to demonstrate analogue modulation of at least 4 GHz. The real-time

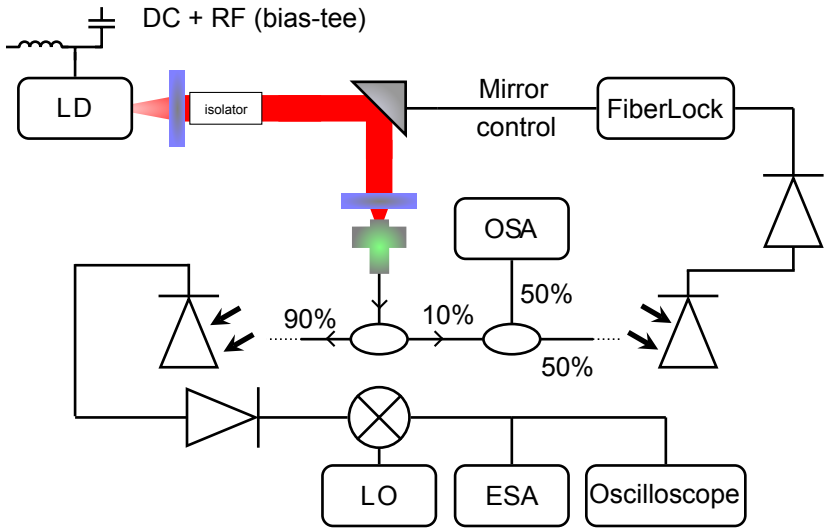

Figure 4.1 *The measurement setup used for laser characterization. LD is the laser diode under test, OSA is the optical spectrum analyzer, LO is the local oscillator, ESA is the electrical spectrum analyzer and FiberLock is the collimation quality locker.*

measurement of these spectra were limited by the fastest available oscilloscope, 2.5 GHz Agilent (Keysight) DSO9254A (20 Gs/s). The digital modulation spectra was measured by modulating the chips with an Advantest D3186 PPG (maximum 12.5 Gbps) using a Rohde & Schwarz SMR20 as the external signal generator. The fastest modulation that is still visible with the oscilloscope is 500 Mbps. However, the spectral broadening under modulation indicates that much higher modulation speeds should work as well.

In the probing setup, delivering enough signal strength becomes an issue when the frequencies increase. The contact between the HF probe and the laser chip are non-ideal, and also impedance mismatch becomes an issue. These problems can be solved for packaged lasers by designing an impedance matching circuit and minimizing the distances the high frequency electrical signal has to travel outside a coaxial cable. However, in the characterization setup employed in this work the only straightforward way was to increase the signal amplitude much higher than what would normally be needed.

5. RESULTS

In this chapter the major results obtained from both simulations and experiments are presented. The experimental results include in-house results from different stages of measurement setup development. The simulation results are compared with the experiments to confirm the validity of the models used.

5.1 Model Validity and Differences

In this section differences between the TMMs used in this thesis are shown. The differences arise from both the formulation and the implementation of solving.

Whenever any numerical simulations are implemented, it is convenient to determine whether their results agree with results that can be analytically calculated. Converging to the analytical solutions gives the model a basic validation. For laser cavities these analytical results are usually the mirror losses of a Fabry–Pérot laser

$$\alpha_m = \frac{1}{2L} \ln\left(\frac{1}{R_1 R_2}\right), \tag{5.1}$$

and the corresponding mode spacing

$$\Delta\lambda = \frac{\lambda_0^2}{2Ln_g + \lambda_0}, \tag{5.2}$$

where $n_g = n_{\text{eff}} - \lambda \frac{dn_{\text{eff}}}{d\lambda}$ is the effective group index. All the TMM implementations pass these basic tests and there are only small variations in the results due to numerical errors.

It is convenient to define a set of characteristics describing the stability and side mode suppression of in laser. These are the side mode suppression ratio (SMSR), the (normalized) side mode loss difference (SMLD) and the (normalized lasing) mode loss difference (MLD). SMSR can be approximated for a single-mode DBR

laser by [73]

$$\mathrm{SMSR} \approx 10 \log_{10} \left(\frac{\Delta\alpha + \Delta g}{\delta_G} + 1 \right), \tag{5.3}$$

where $\Delta\alpha$ is the optical loss difference between the lasing mode and the strongest competing mode, Δg is the modal gain difference between those modes, and δ_G is the net modal gain for the lasing mode. This SMSR value is not valid for a general structure, but nonetheless it will be compared with the other characteristics later in this chapter.

SMLD is analogous with SMSR, but is a dimensionless quantity and doesn't change with the type of laser. It is defined simply by

$$\mathrm{SMLD} = \Delta\alpha L, \tag{5.4}$$

where $\Delta\alpha$ is the optical loss difference between the lasing mode, or between the weakest lasing mode for a multi-wavelength laser case, and the strongest competing mode.

An extension to this quantity is the MLD, which describes the mode balance between the lasing modes in a multi-wavelength laser. It is defined similarly by

$$\mathrm{MLD} = \Delta\alpha_l L, \tag{5.5}$$

where $\Delta\alpha_l$ is the optical loss difference between the strongest and weakest lasing modes.

In Figure 5.1 the difference in stability of the two TMM formulations introduced in Section 2.4.1 and Section 2.4.2 is shown when two different types of cavity asymmetries are induced into the simulations. The stability is illustrated by two quantities, by SMLD, and by the difference frequency f_{diff}. f_{diff} is the frequency difference between the two lasing modes.

Figure 5.1 a) corresponds to an imperfect cleaving of the laser, a phenomenon very common in device fabrication and processing. The result shows more instability with coupled wave implementation. This is against experimental results: lasing devices with good behavior have been characterized with greater (and asymmetric) end section cleaving than the coupled wave result gives as the limit for working devices.

In Figure 5.1 b) the cavity n_{eff} is tuned asymmetrically, i.e. in only a limited part

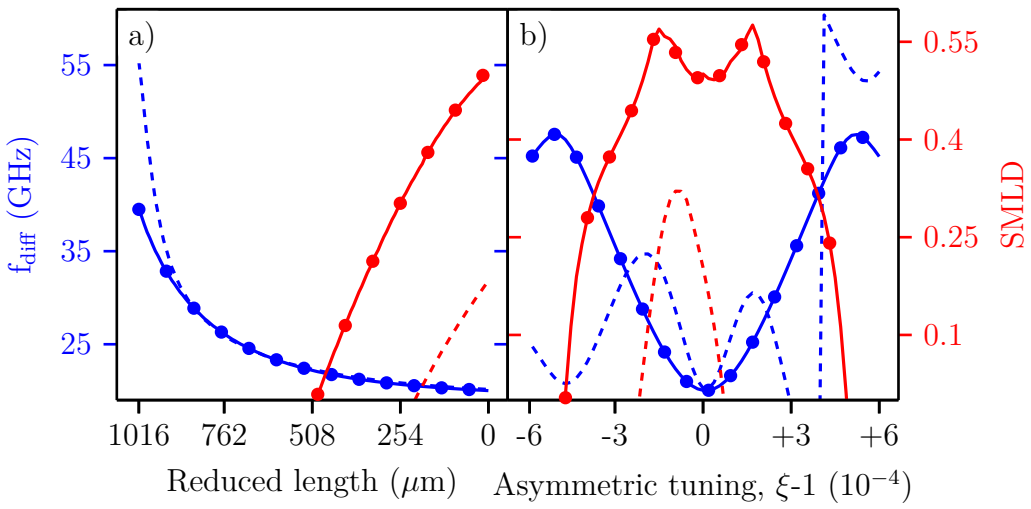

Figure 5.1 *Effect of induced cavity asymmetries on f_{diff} and SMLD. Solid lines (—— and ——) are obtained with the fundamental transfer matrix model, dashed lines (- - - and - - -) are obtained with the coupled wave model and dots (• and •) are obtained with the fundamental method with adjusted solving using matrix resonances. The dots are within numerical error from the solid lines. Red lines give SMLD variation and blue lines give f_{diff} variation. In a) the length of the device is reduced from both ends equally. The total length of the device is 1.53 mm. In b) the n_{eff} of the laser is tuned asymmetrically. SMLD value below 0 means that the two desired modes are not the dominant ones.*

of the cavity. The result shows similar behavior as the imperfect cleaving. The difference is that now f_{diff} also changes differently with the induced asymmetry. This means either that there is a difference in how the two formulations handle cavity asymmetries, or that the way the n_{eff} tuning is implemented is not equivalent, or both. For the devices characterized in this thesis, the TMM formulation of Section 2.4.1 has shown results that fit the experimental data better.

5.2 Internal Field Evaluation

Using Equation (2.1) the flatness from the internal field distribution is evaluated. To get a correct field distribution and flatness value, the internal field has to be evaluated on a 1D longitudinal mesh of certain resolution. The needed resolution depends on the wavelength of the lasing mode. The Nyquist rate gives a limit after which there is no differences in the evaluated fields (twice the highest spatial frequency component, or reciprocally half the lowest wavelength in the system). This is demonstrated in Figure 5.2 with an internal field flatness evaluation for an example laser structure. Indeed, after the Nyquist rate limit the field flatness (and distribution) stays constant (area a). An interesting area in the flatness curve, between the perfect and zero reconstruction domains, is the partial reconstruction domain

where the internal field is evaluated partially correctly (area b). This domain is between the sampling resolution given by the Nyquist rate ($\Delta x_{\mathrm{Nyquist}}$) and the highest homogeneous dimension in the matrix describing the laser structure ($\Delta x_{\mathrm{maxdim}}$). In a Bragg gratings such as used in this thesis, both of these mesh quality threshold values are linked to the wavelength. Field distributions in all three different domains are also shown in the right panel.

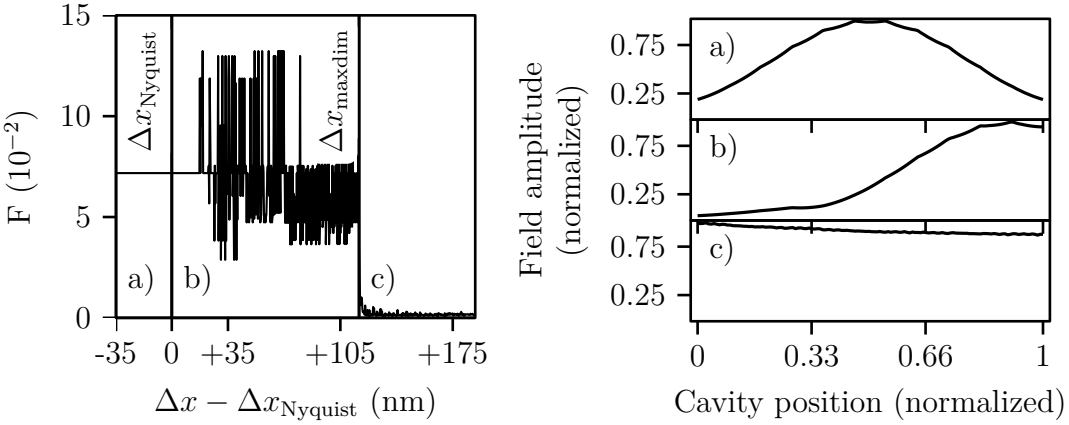

Figure 5.2 *Field flatness around the limit resolution given by the Nyquist rate ($\Delta x_{Nyquist}$). Sample field distributions from all three of the reconstruction domains are also plotted: a) perfect, b) partial, and c) zero reconstruction. The device has a distributed phase shift structure with 10 equal phase shifts and the sum of the phase shift strengths is $\sum \theta_k = \pi/2$ to achieve 1-mode operation [74, 75].*

The importance of this fundamental limit for numerical simulations is two-fold. First, it is easy to determine what the resolution of the simulation mesh must be for it to be accurate. Second, accuracy can be achieved with least amount of calculation effort.

5.3 Two-wavelength Emission

Emission of laser radiation at two separate, quasi-phase-locked modes is one of the main goals of the research in this thesis. In this Section a simulated spectrum is compared with an experimental one, and a yield analysis for dual-mode lasing is presented. The comparison shows good agreement between the models and the experimental behavior of the devices.

Figure 2.5 compares simulation results from PICS3D [76] software with corresponding experimental data. The mode separation is correct, but the emission wavelengths

differ somewhat. This is due to small inaccuracies in the fabrication process of the diode, as well as the temperature dependence of the effective index and gain spectrum. The mode separations are exactly the same, which is a good indicator that the used approach in achieving predictable and stable mode separation in dual mode emission is working.

One important aspect of fabricating the chips is the yield, which is what percentage of the devices can be expected to work. Assuming that the diode fabrication process is perfect, the only aspect affecting the operation stability is the random facet position [77] resulting from cleaving. Using normalized mirror loss difference (MLD) values of 0.05 as the guideline [78], in Figure 5.3 the yield with various configurations of end facet reflectivities has been analyzed. A device is considered within the yield if the mirror losses of both lasing modes are smaller than of any competing mode near the center wavelength by the amount given in the guideline.

5.4 Structural Effects

Determining the effects of various structural parameters of the lasers is of great importance. They are important in deriving guidelines for device design and fabrication. In this section the laser figure of merit dependencies on structural parameters are outlined.

The lasing characteristics: side mode suppression ratio (SMSR), SMLD and F as a function of κL are presented in Figure 5.4. Both the SMSR and the SMLD reach their optimum values for lower κL value than the value for which F is worst. Thus in terms of these quantities the chosen κL is always a compromise. The maximum values of SMLD and SMSR are at different values of κL due to the approximations used in the SMSR evaluation [73]. These quantities are used to determine the characteristics of a single-mode laser. In order to estimate the stability of dual-mode emission, both modes have to be considered. However, in the case of a symmetrical structure, both modes have the same mirror losses and field distributions.

When the effective refractive index distribution is symmetrical the longitudinal mode envelopes of both lasing modes overlap almost perfectly. The modes compete for the gain in the same areas of the laser. This leads to very unstable operation around this operating point [79]. To get more stable devices, the modes should overlap significantly less. For the dual-wavelength laser this is the case when the effective refractive index distribution is disturbed and there is an asymmetry. This is also one of the reasons why the devices fabricated have consistently higher difference frequency between the two modes than the ideal simulations predict.

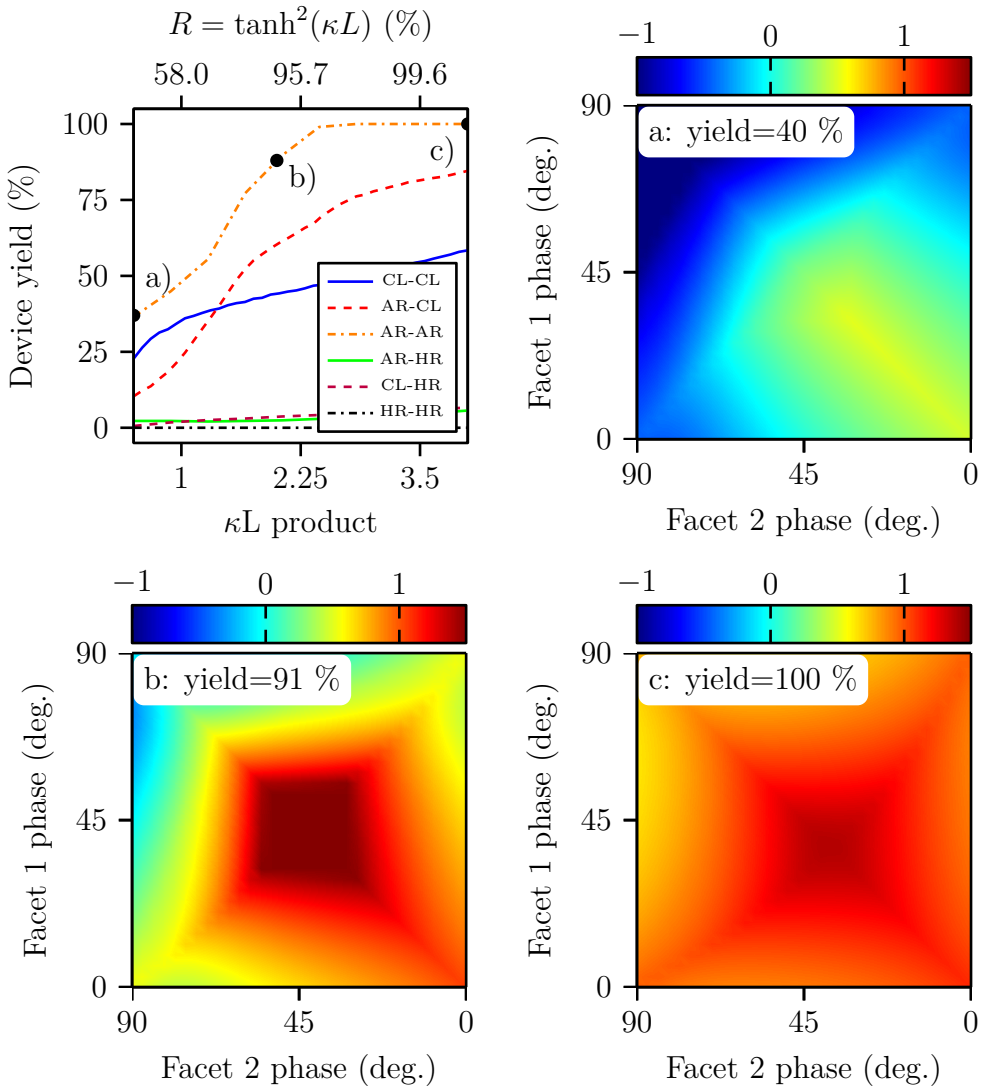

Figure 5.3 *Yield values with changing coupling strength for several end facet combinations. The facet type acronyms stand for cleaved (CL), anti-reflection (AR) and high reflection (HR). The best yield is achieved with AR-AR combination because in that case the facets have the least effect, and the stability is due to the grating. The SMLD yield maps for the three points highlighted with black dots on the AR-AR curve are plotted in the contour plots. The facet phases in degrees are 0 for perfectly matching phase and 90 for perfectly anti-matching phase.*

Similarly the dependence of the difference frequency of the dual mode emission on the structural parameters, namely the length and the coupling coefficient, are important. In Figure 5.5 the effect of device length and coupling coefficient on the difference frequency is shown. The length of the device determines the rough mode separation, the changes in the coupling coefficient can be used for fine tuning the separation frequency. In the scale of the figure, the effect of κ is negligible on the mode separation. As mentioned before, these simulations give the minimum

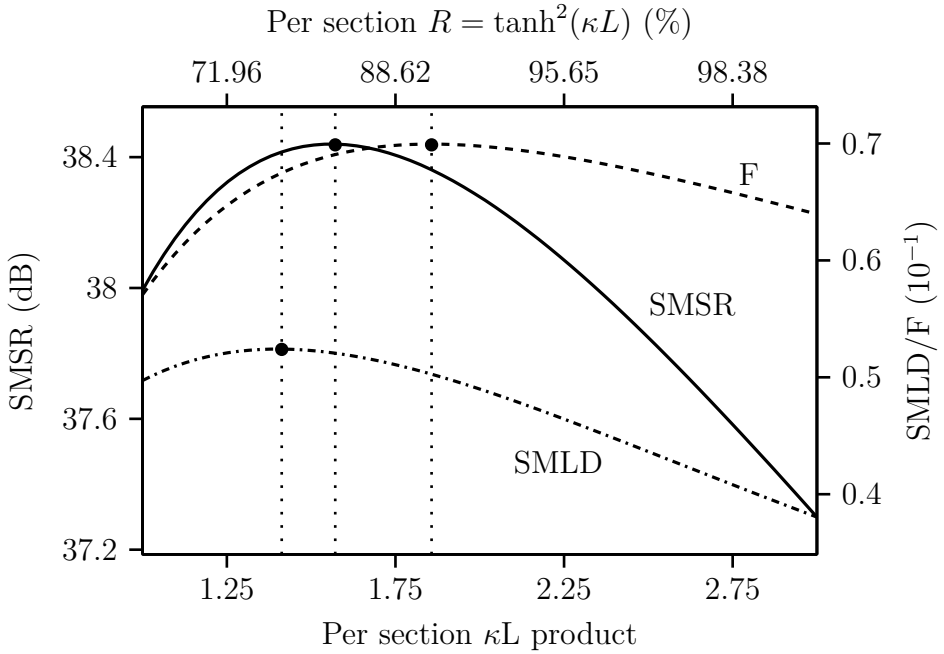

Figure 5.4 *Effect of changing κL on flatness, SMLD and SMSR. The black dashed lines and the corresponding dots are related to the maxima of each curve.*

achievable mode separation for the laser.

For the other quantities in Figure 5.5 the effect of κ is more evident. SMLD shows a minimum area with approximately equal κL value. SMSR has a minimum value with approximately the same κL product but with only short length. As in Figure 5.4, the worst flatness value is at higher κL value than the optima of SMSR and SMLD.

5.5 Laser Tuning

By tuning the effective index of one of the laser sections a change in f_{diff}, as well as mode balance quantities is induced. This is illustrated by 2-D tuning maps in Figure 5.6. For a more detailed view, the dotted lines from the maps also shown in Figure 5.7 as line plots. When the laser is tuned symmetrically, the effect on the difference frequency is very small in comparison to when the tuning is asymmetrical. One reason for this is that the asymmetric tuning changes the internal field distributions of the two modes more. That is, the internal fields of the modes become spatially more separated, reducing the mode overlap. This also leads to better SMLD and MLD values compared to the symmetric tuning case.

Even though tuning the laser symmetrically yields much lower change in the f_{diff},

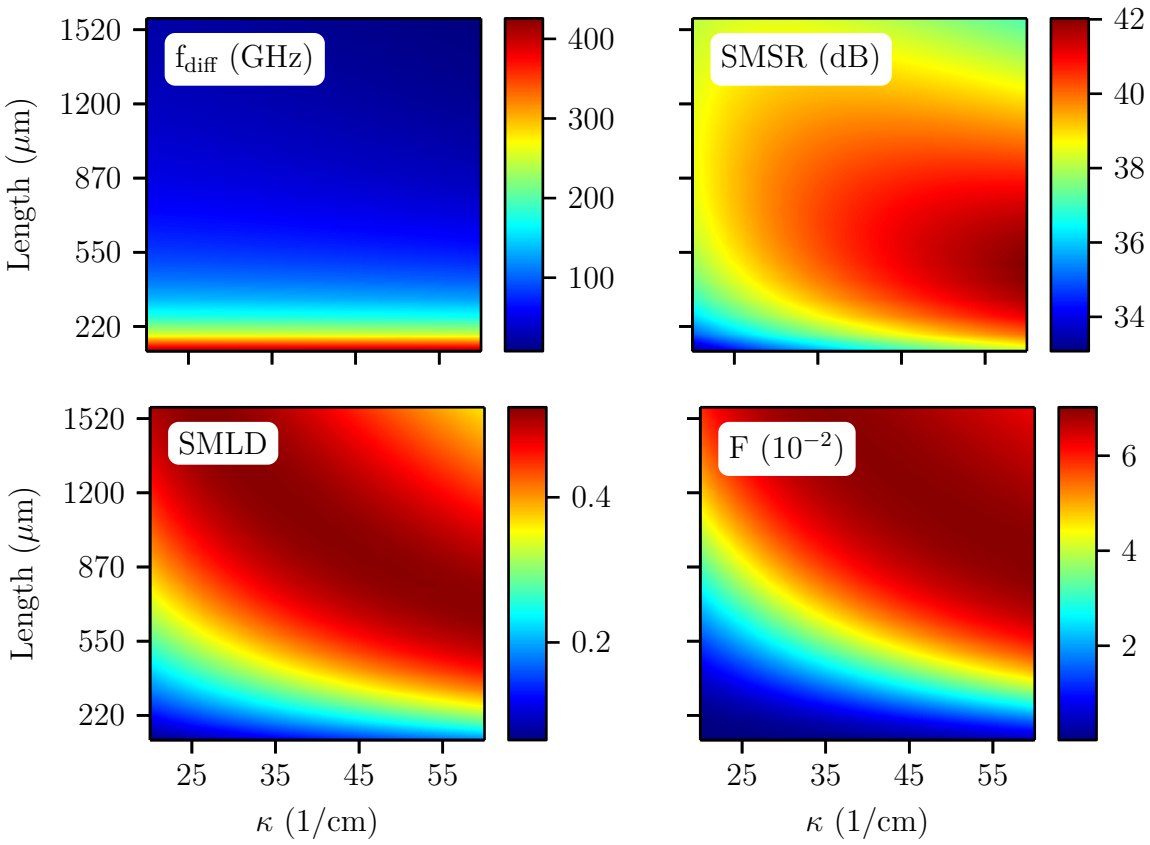

Figure 5.5 *f_{diff}, SMSR, SMLD and F dependencies on device length and κ.*

its effect on the mode stability is much greater: the dual mode lasing is disturbed with lower tuning depth than what is required with the asymmetric type. This indicates that for the best tuning results, the laser should be tuned asymmetrically. Furthermore, using only one type of tuning enables easier prediction of the effects of tuning.

The relatively high flatness value for all tuning types shows that the cavity field intensity envelope is concentrated, and SHB becomes a problem with higher pumping. However, a more revealing quantity for dual-wavelength lasers is the (field) intensity overlap (η_{int}). This gives the overlap relation between the longitudinal field distributions of the two lasing modes. If the quantity is high (close to unity), then the modes are highly overlapping. This leads to bistable behavior and should be avoided. The effect of tuning on η_{int} is illustrated in Figure 5.8. High symmetry breaking leads to a low field overlap.

There are, however, some problems associated with symmetry breaking in the longitudinal effective index distribution. Severe asymmetry starts inducing mode hopping. A simple illustration of this mechanism is given in Figure 5.9. In the figure

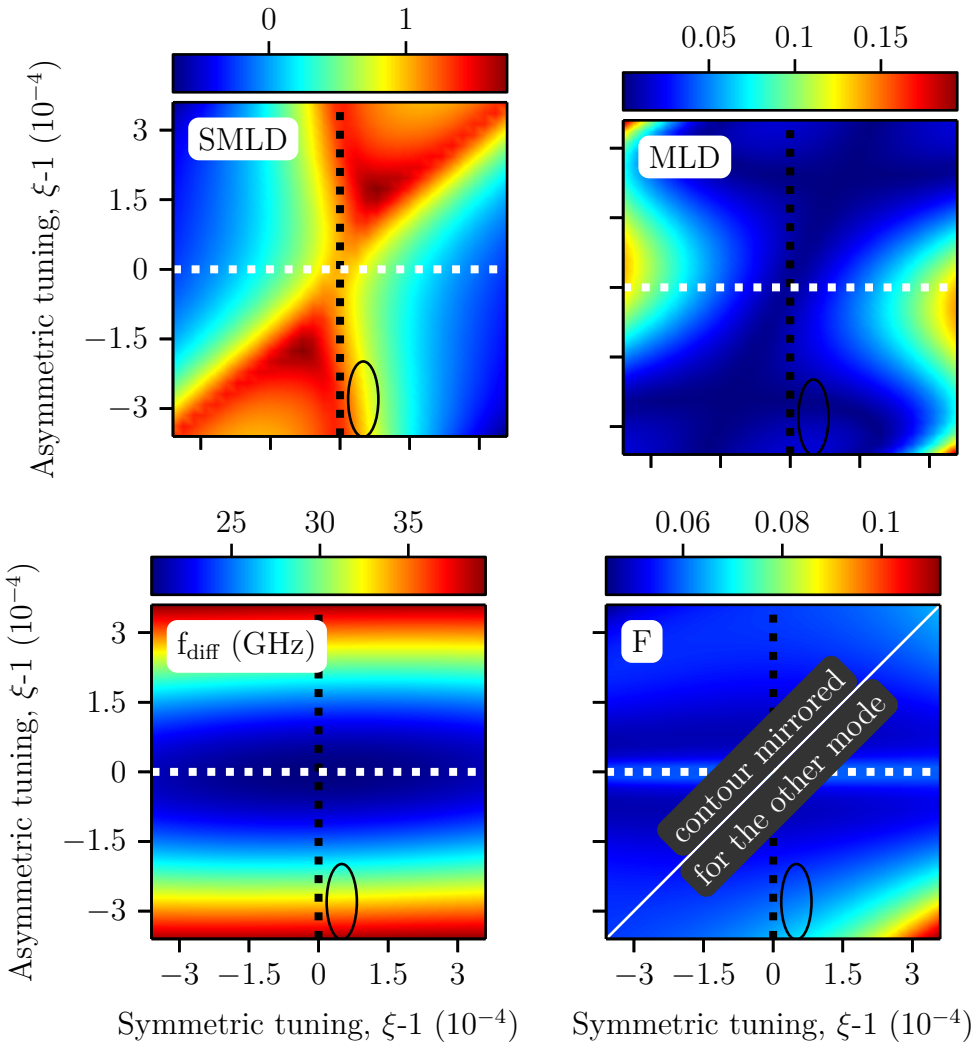

Figure 5.6 *Simulated SMLD, MLD, f_{diff} and F values for a typical multisection laser when it is tuned both symmetrically and asymmetrically. Black and white dotted lines correspond to lines with full and empty markers in Figure 5.7, respectively. F contour mirrors along the drawn line when the value is evaluated for the other mode. The drawn ellipse highlights one typical measurement scenario: increasing bias current asymmetrically decreases the difference frequency. See Figure 5.10 for a comparison with experimental results.*

parts of the laser are symmetrically tuned. In the non-tuned position the stop bands of all parts of the laser are aligned, and the device is working in the ideal domain. However, when a tuning is introduced, the center wavelength of the tuned parts shifts accordingly, and we see the drift in the reflectivity spectra as the stop bands of the tuned and non-tuned parts separate. When there is a dichotomy between the stop bands, even a small change in the tuning induces a mode hop. This means that the device is unstable when the tuning depth is too high.

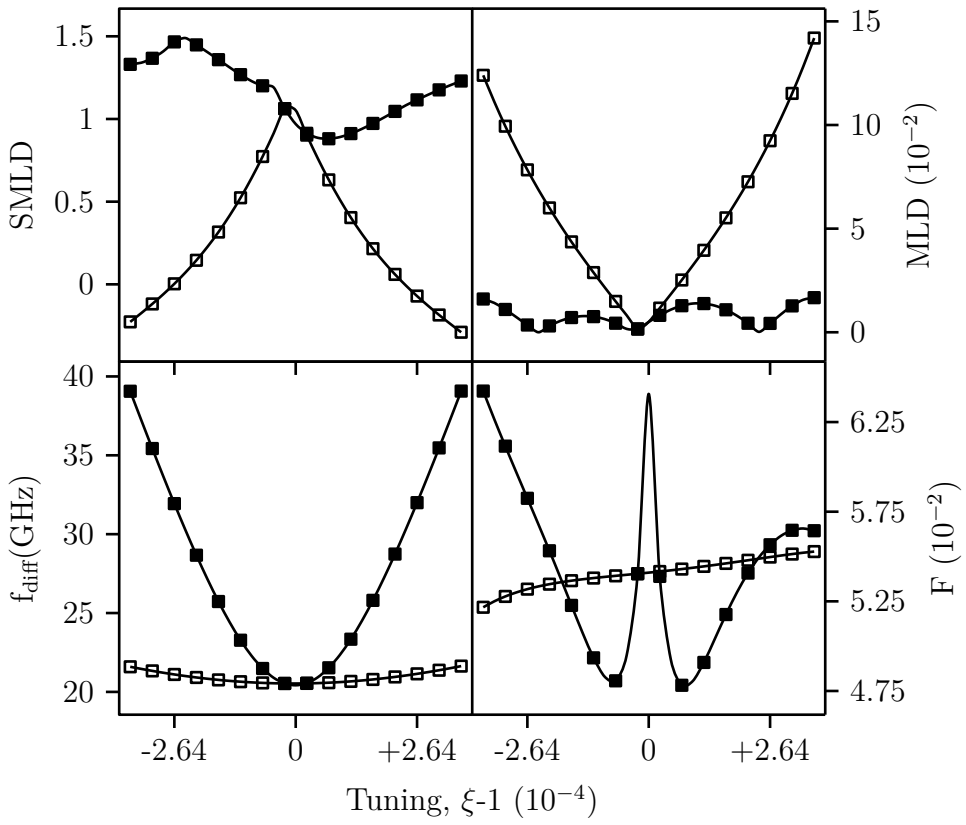

Figure 5.7 *Values along the dotted lines in Figure 5.6. The lines with solid marks correspond to the black dotted lines and the lines with empty marks to the white ones.*

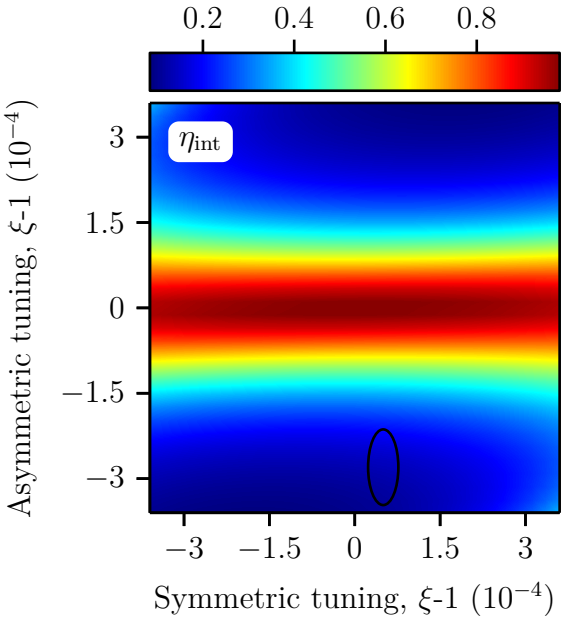

Figure 5.8 *Field intensity overlap when the laser is tuned symmetrically and asymmetrically. The drawn ellipse is the same as in Figure 5.6.*

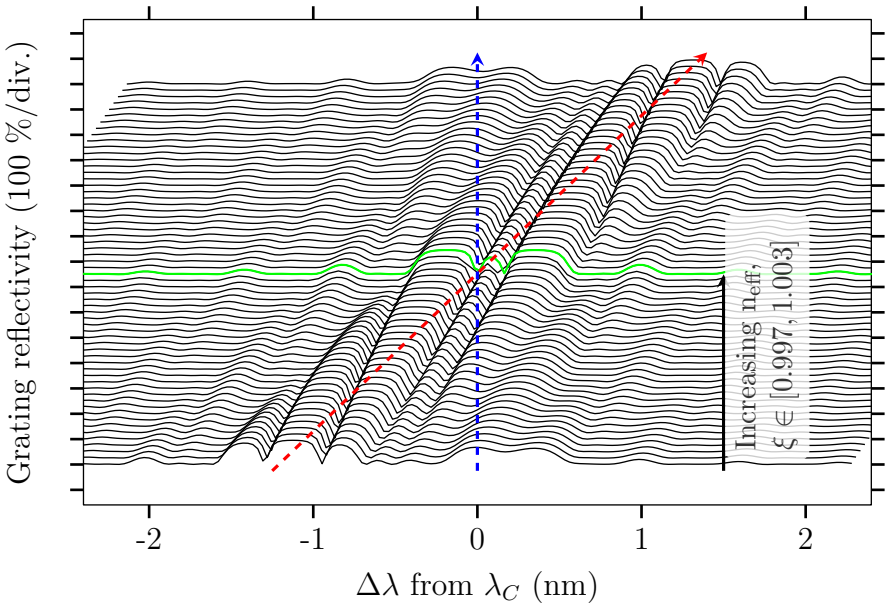

Figure 5.9 *Separation of the stop-bands between tuned and non-tuned parts of a laser. The red dashed line follows the stop band corresponding to the tuned, and the blue one to the non-tuned part of the laser. The stop-band of the case when $\xi = 1$ is shown in green.*

To counteract this instability, the tuning scheme should be such that all the parts of the laser have effective indices close enough to each other, and thus central wavelengths.

5.5.1 Measurement Results

The tuning capabilities of chips fabricated for the ICT FP7 DeLight project have been measured. In Figure 5.10 a typical behaviour of a dual-mode chip under varying bias currents is shown. The change in only one bias current induces a change in the difference frequency as well as the mode balance. Changing two bias currents keeps the mode balance as well as the difference frequency constant. Comparing this result with Figure 5.7 it can be seen that the two different sections of the laser are in different parts on the tuning curve. Increasing I_2 decreases f_{diff}: that section is operating left of the neutral position in Figure 5.7, and vice versa for I_1.

Using a similar approach the operating currents for the rest of the legacy DeLight chips have been determined.

The beat signal in the electrical spectrum with varying bias currents has been plotted in a similar fashion in Figure 5.11 a). The beat signal frequency corresponds to the mode separation between the two modes, but the signal has been down-mixed with a LO and a mixer because the beat signal frequency was higher than the ESA

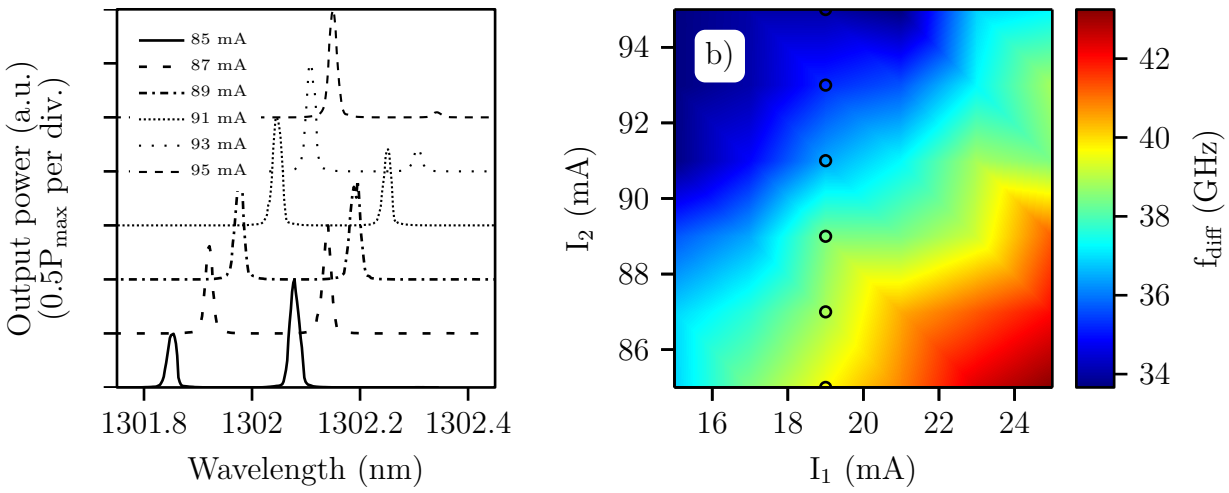

Figure 5.10 *a) Typical optical spectra with one varying bias current. b) Corresponding difference frequency map when two bias currents are changed. The operating points for the optical spectra in a) are marked on the bias map b) with circles.*

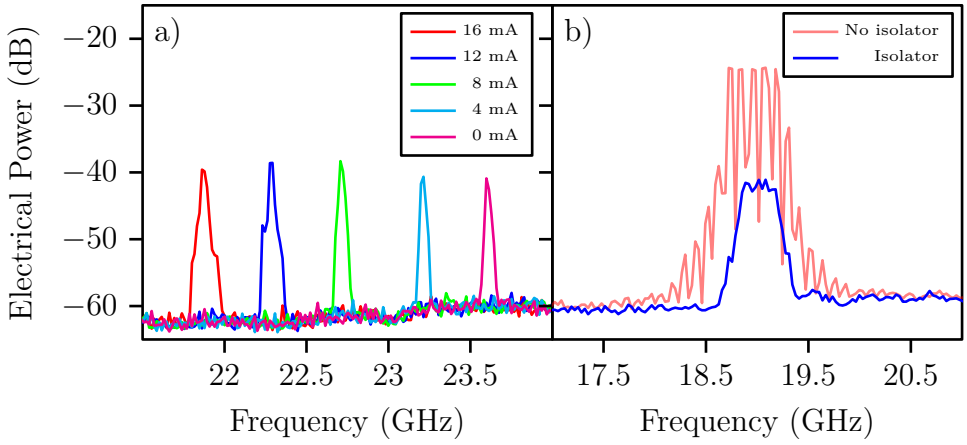

Figure 5.11 *Typical ESA results. a) shows a typical f_{diff} change by an asymmetric bias current tuning. b) shows the effect of an isolator on the spectrum. a) uses down-mixing and b) direct difference frequency detection.*

bandwidth. The beat signal is detected even with relatively poor mode balance, and typically the available tuning in the mode separation is in the range several gigahertz.

In addition, the effect of leaving out the optical isolator from the measurement setup is shown in Figure 5.11 b). The spikes in the non-isolated line are due to resonances between the collimation setup lenses. Additionally, it is possible that the reflected beams couple back into the laser diode and disturb the operation. The figure is a good example why optical isolation is a requirement in coupling light into a fiber.

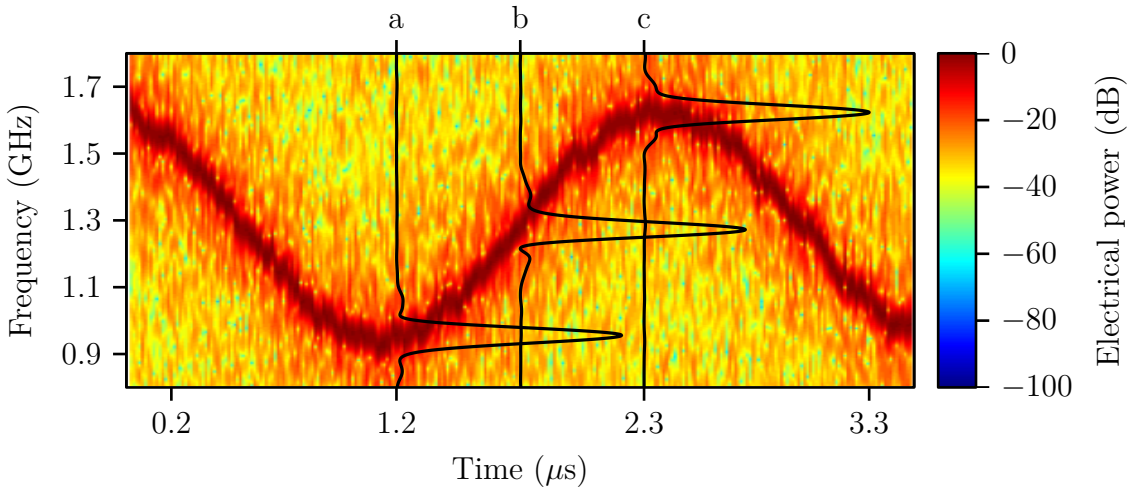

Figure 5.12 *Spectrogram for low frequency analogue tuning at 400 kHz. The overlaid line plots a–c are the window Fourier transforms of the spectrograms in arbitrary linear scale around the time slots marked by the letters. The spectrogram scale is normalized and logarithmic.*

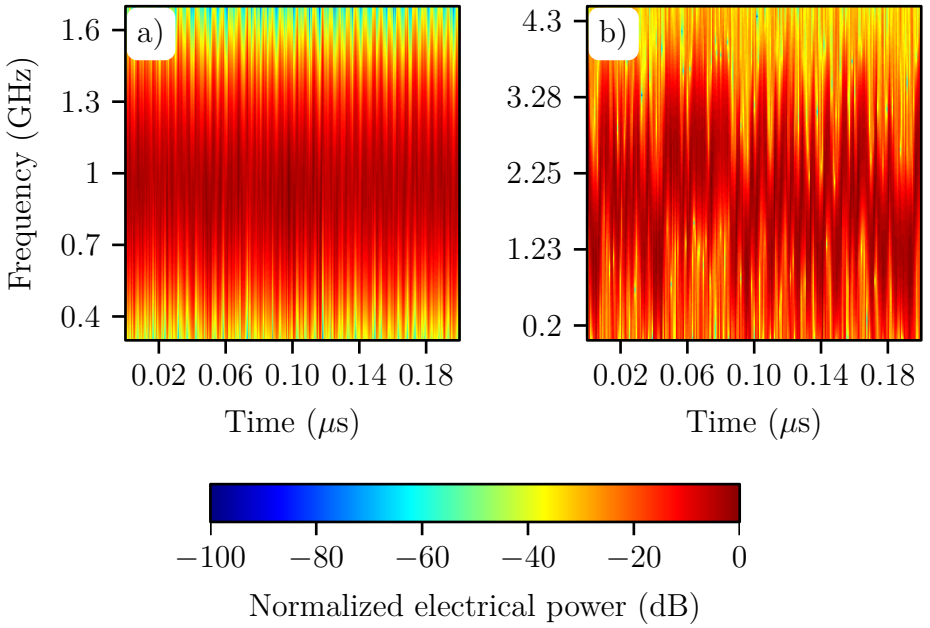

Figure 5.13 *Spectrograms for analogue and digital tuning at higher frequencies. a) 200 MHz analogue signal. b) 500 MHz digital signal.*

By tuning with varying frequencies, not just DC, the speed limits for the frequency difference tuning can be determined.

When tuning with analogue signals there are side bands due to Bessel functions. At lower frequencies of the analogue signal this means that the beat frequency *follows*

the tuning signal if the linewidth of the beat signal is much larger than the tuning frequency. In this case the modulation index is very high. Modulation index is defined as

$$h = \frac{\Delta f}{f_m}, \tag{5.6}$$

where Δf is the peak frequency deviation, and f_m is the modulation frequency.

Using a digital signal for tuning results in two discrete beat signal frequencies. The analogue low frequency case, with slices of the spectrogram plotted for clarity, is illustrated in Figure 5.12. The modulation index h in the figure is approximately $\frac{700\text{MHz}}{2\cdot 400\text{kHz}} = 875$. The factor 2 is because Δf is defined as the deviation from the beat signal frequency. This value of h means that there are hundreds of modulation sidebands in the span of 700 MHz. In the figure the linewidth of the beat signal is larger than the f_m and these modulation sidebands overlap. This results in such a spectrogram where the beat signal frequency follows the modulation signal. The ripples in the overlaid line spectra are not the side bands from the modulation, but result from the limited temporal width of the window Fourier transform.

Figure 5.13 shows the spectrograms at higher frequencies, both for digital and analogue tuning type. The resolution is limited by the 2.5 GHz oscilloscope. Because of the oscilloscope bandwidth the beat signal is down-mixed with a LO and a mixer to that frequency range. Faster tuning speeds are also visible but only indirectly from the electrical spectrum broadening. There is only an analogue tuning case at the lower frequency range because the minimum bit rate from the D3186 PPG is 150 Mbps.

5.6 Optimization Studies

By using a heuristic optimization scheme introduced in Section 3.2, it is possible to reach desired mode separation and suppression even with several modes.

In Figure 5.14 the evolution of the fitness value during one optimization run is plotted. The aim is to get a structure that has 4 modes with equal mirror losses. This was chosen as the goal in order to have several different f_{diff} values in one cavity. This could enable the flattening of the modulation response curve, which would show up as several PPR peaks in Figure 2.7. Changing the fitness function to include η_{int} minimization (from a) to b)) makes the fitness converge faster. On the other hand, giving additional degrees of freedom (arbitrary phase shifts) makes the behavior of the fitness value much more erratic. However, there is still a clear

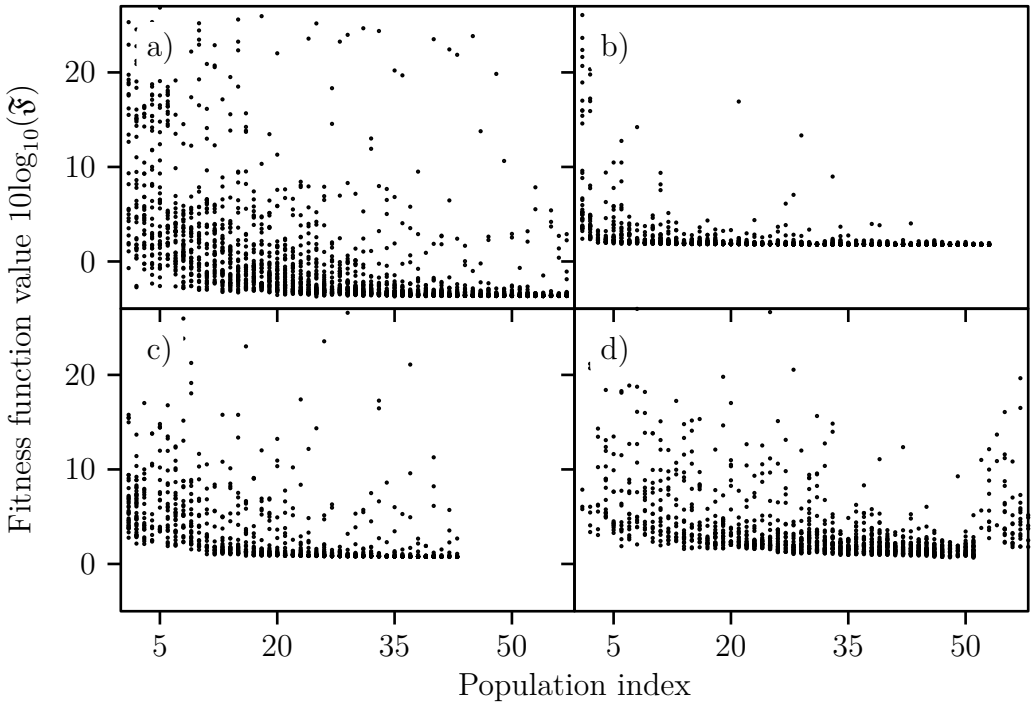

Figure 5.14 *Evolution of $\mathfrak{F}$ during optimization for a 4-mode device when a) only the MLD and the SMLD are the goal function and only the lengths of different sections are varying; b) η_{int} is included in the goal function; c) phase shift strengths can also change; d) number of phase shifts is increased from 5 to 9.*

minimum where the optimizer converges. Finally, adding further degrees of freedom (9 phase shifts and accordingly 10 sections of varying lengths) slows down the convergence and additionally makes the convergence point much broader. This means that there are many candidates with similar performances, but the input vectors of those candidates differ. Because of this the optimizer tries to find the global minimum around several good, but differing input parameter sets. The jump in the fitness value distribution in Figure 5.14 d) after population number 50 corresponds to a restart of the algorithm.

The corresponding mirror loss spectra for the best candidates from Figure 5.14 are shown in Figure 5.15. Interestingly, adding the overlap minimization requirement (change from a) to b)) does not change the structure the optimizer converges to, and in fact the value of η_{int} stays the same. On the other hand, when the strength of the phase shifts is also set as a free variable, the resulting structure and spectrum change drastically. This indicates that to have a minimal η_{int} along with stable mode balance, using a constant phase shift amount is not the best approach. Finally, increasing the number of sections in the candidates yields a different spectrum. Because the convergence point of the fitness value for d) is much broader, several

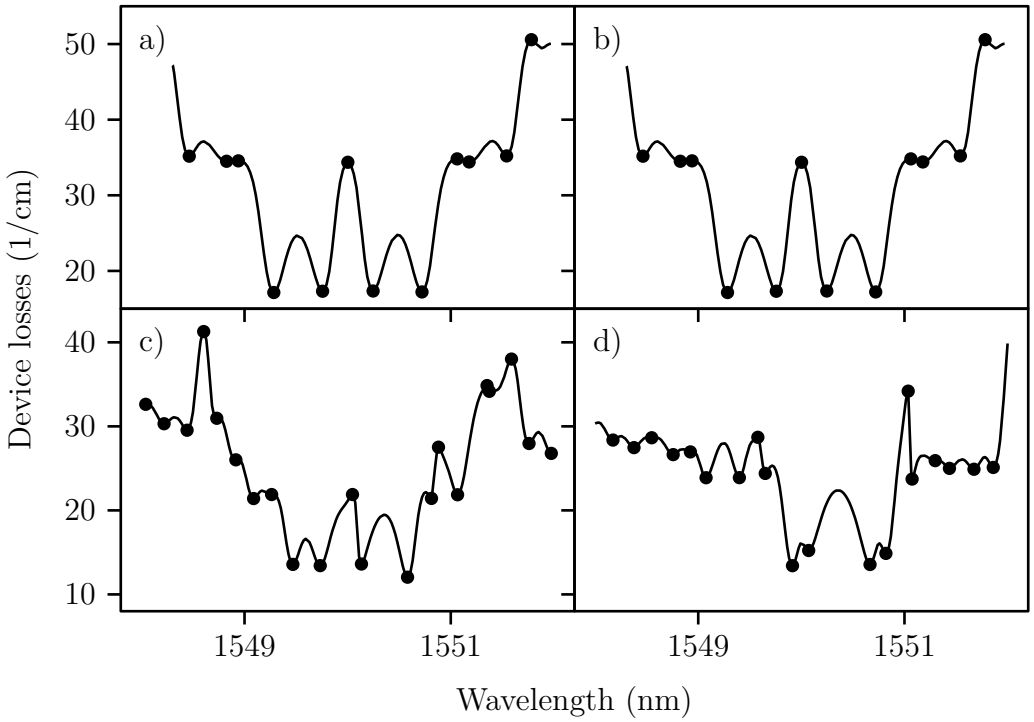

Figure 5.15 *Device loss spectra from the optimization candidates. The order of a)–d) is the same as in Figure 5.14. The dots are the cavity modes.*

different candidates could also have been chosen. Even though c) and d) spectra appear to be more erratic, their characteristics for stable multi-mode emission are better when compared with the spectra of the optimal structures from a) and b) cases.

Even though the behavior of these optimization candidate devices is interesting, the structures are very complex. Because of this, there is no experimental data from fabricated devices with corresponding structural parameters. The results, however, show that using heuristic optimization methods is a valid procedure in finding structures that fulfill certain performance criteria. Even solving the inverse problem of arriving to a laser structure from a given, arbitrary, output or reflection spectra becomes possible.

6. SUMMARY

Two TMM approaches for DFB-LD design have been presented. The underlying theory and relevant derivations were shown. The application areas for dual-wavelength lasers were also discussed on a basic level with emphasis on the application of the DFG. What role the lasers play in those application areas was further highlighted.

The experimental setup used in the thesis was described explicitly at its various development stages. It was used successfully to achieve a good fiber coupling with relative ease, and the setup can be used on a wide variety of laser chips of various dimensions and LD mounting configurations.

The results between the two TMM formulations were compared, with clear differences between them. The differences, albeit drastic, were associated with the differences in the formulation: explicit values for each mirror pair in the first formulation, versus an averaged value for each part of the laser in the second. The simulation results obtained from the former TMM formulation were then compared with the experimental data, and correspondences were highlighted. Further, various structural parameter dependencies were presented.

Some future possibilities were also outlined. Using sophisticated optimization algorithms, it was shown that LD structure design candidates fulfilling arbitrary criteria were a possibility, at least design-wise. As an extension to this, statistical analysis can be used to have possibly more realistic yield figures than the ones presented in the thesis. This, however, is beyond the scope of this thesis, and a subject for future work.

BIBLIOGRAPHY

[1] K. E. Niebuhr, "Generation of laser axial mode difference frequencies in a nonlinear dielectric," Applied Physics Letters **2**, 136–137 (1963).

[2] E. H. Bernhardi, K. O. van der Werf, A. J. F. Hollink, K. Wörhoff, R. M. de Ridder, V. Subramaniam, and M. Pollnau, "Intra-laser-cavity microparticle sensing with a dual-wavelength distributed-feedback laser," Laser & Photonics Reviews **7**, 589–598 (2013).

[3] X. Chen, Z. Deng, and J. Yao, "Photonic generation of microwave signal using a dual-wavelength single-longitudinal-mode fiber ring laser," Microwave Theory and Techniques, IEEE Transactions on **54**, 804–809 (2006).

[4] C.-L. Wang and C.-L. Pan, "Tunable multiterahertz beat signal generation from a two-wavelength laser-diode array," Opt. Lett. **20**, 1292–1294 (1995).

[5] A. Einstein, "Strahlungs-emission und absorption nach der quantentheorie," Deutsche Physikalische Gesellschaft **18**, 318–323 (1916).

[6] O. Svelto, *Principles of Lasers* (Springer, 2009), 5th ed.

[7] S. L. Chin, H. Xu, Y. Cheng, Z. Xu, and K. Yamanouchi, "Natural population inversion in a gaseous molecular filament," Chinese Optics Letters **11**, 013201 (2013).

[8] W. P. Dumke, "Interband transitions and maser action," Phys. Rev. **127**, 1559–1563 (1962).

[9] I. Vurgaftman, J. Meyer, and L. R. Ram-Mohan, "Band parameters for III–V compound semiconductors and their alloys," Journal of Applied Physics **89**, 5815–5875 (2001).

[10] W. Bragg, "The diffraction of short electromagnetic waves by a crystal," Proceedings of the Cambridge Philosophical Society **7**, 43–57 (1913).

[11] P. Agraval, *Semiconductor Lasers* (1993).

[12] C. L. Tang, H. Statz, and G. deMars, "Spectral output and spiking behavior of solid–state lasers," Journal of Applied Physics **34**, 2289–2295 (2004).

[13] A. Moser, E.-E. Latta, and D. J. Webb, "Thermodynamics approach to catastrophic optical mirror damage of AlGaAs single quantum well lasers," Applied Physics Letters **55**, 1152–1154 (1989).

[14] H. Ghafouri-Shiraz, B. S. K. Lo, and C. Y. J. Chu, "Structural dependence of three-phase-shift distributed feedback semiconductor laser diodes at threshold using the transfer matrix method," Semiconductor Science and Technology **9**, 1126–1132 (1994).

[15] H. Soda, Y. Kotaki, H. Sudo, H. Ishikawa, S. Yamakoshi, and H. Imai, "Stability in single longitudinal mode operation in GaInAsP/InP phase-adjusted DFB lasers," IEEE Journal of Quantum Electronics **23**, 804– 814 (1987).

[16] A. Klehr, J. Fricke, A. Knauer, G. Erbert, M. Walther, R. Wilk, M. Mikulics, and M. Koch, "High-power monolithic two-mode DFB laser diodes for the generation of THz radiation," IEEE Journal of Selected Topics in Quantum Electronics **14**, 289–294 (2008).

[17] F. Pozzi, R. M. De La Rue, and M. Sorel, "Dual-wavelength InAlGaAs–InP laterally coupled distributed feedback laser," IEEE Photonics Technology Letters **18**, 2563–2565 (2006).

[18] J. Shive, "The phototransistor," Bell Lab. Record **28**, 337 (1950).

[19] G. Lucovsky and P. H. Cholet, "GaAs, a sensitive photodiode for the visible," Journal of the Optical Society of America **50**, 979 (1960).

[20] Y. Sasaki, A. Yuri, K. Kawase, and H. Ito, "Terahertz-wave surface-emitted difference frequency generation in slant-stripe-type periodically poled LiNbO3 crystal," Applied Physics Letters **81**, 3323–3325 (2002).

[21] S. Chandrasekhar, J. Campbell, A. Dentai, C. Joyner, G. Qua, and W. SNELL, "Integrated waveguide p-i-n photodetector by MOVPE regrowth," IEEE Electron Device Letters **8**, 512–514 (1987).

[22] K. Giboney, M. J. W. Rodwell, and J. Bowers, "Traveling-wave photodetector theory," IEEE Transactions on Microwave Theory and Techniques **45**, 1310–1319 (1997).

[23] H. Ito, S. Kodama, Y. Muramoto, T. Furuta, T. Nagatsuma, and T. Ishibashi, "High-speed and high-output InP-InGaAs unitraveling-carrier photodiodes," IEEE Journal of Selected Topics in Quantum Electronics **10**, 709–727 (2004).

[24] C. Lim, A. Nirmalathas, D. Novak, R. Waterhouse, and G. Yoffe, "Millimeter-wave broad-band fiber-wireless system incorporating baseband data transmission over fiber and remote LO delivery," Journal of Lightwave Technology **18**, 1355 (2000).

[25] "About | WirelessHD," `http://www.wirelesshd.org/about/`.

[26] M. Stevens and G. Grafton, "The benefits of 60 ghz unlicensed wireless communications," `http://www.sub10systems.com/wp-content/uploads/2011/03/White-Paper-Benefits-of-60GHz.pdf`.

[27] H. Schmuck, "Comparison of optical millimetre-wave system concepts with regard to chromatic dispersion," Electronics Letters **31**, 1848–1849 (1995).

[28] U. Gliese, S. Norskov, and T. Nielsen, "Chromatic dispersion in fiber-optic microwave and millimeter-wave links," IEEE Transactions on Microwave Theory and Techniques **44**, 1716–1724 (1996).

[29] G. Smith and D. Novak, "Broadband millimeter-wave fiber-radio network incorporating remote up/downconversion," in "Microwave Symposium Digest, 1998 IEEE MTT-S International," , vol. 3 (1998), vol. 3, pp. 1509–1512 vol.3.

[30] J. C. Attard and J. E. Mitchell, "Optical network architectures for dynamic reconfiguration of full duplex,multiwavelength, radio over fiber," Journal of Optical Networking **5**, 435–444 (2006).

[31] J. E. Mitchell, "Radio-over-fiber (RoF) networks," in "Broadband Access Networks," , A. Shami, M. Maier, and C. Assi, eds. (Springer US, 2009), Optical Networks, pp. 283–300.

[32] T. Uusitalo, A. Laakso, J. Viheriälä, O. Hyvärinen, L. Toikkanen, and M. Dumitrescu, "Dual-wavelength lasers for difference-frequency generation of thz radiation," (Presented at the 3rd EOS Topical Meeting on Terahertz Science & Technology (TST 2012), 2012).

[33] T. Kampfrath, K. Tanaka, and K. A. Nelson, "Resonant and nonresonant control over matter and light by intense terahertz transients," Nature Photonics **7**, 680–690 (2013).

[34] H.-J. Song, K. Ajito, A. Wakatsuki, Y. Muramoto, N. Kukutsu, Y. Kado, and T. Nagatsuma, "Terahertz wireless communication link at 300 GHz," in "2010 IEEE Topical Meeting on Microwave Photonics (MWP)," (2010), pp. 42–45.

[35] P. Siegel, "Terahertz technology," IEEE Transactions on Microwave Theory and Techniques **50**, 910–928 (2002).

[36] J. F. Federici, B. Schulkin, F. Huang, D. Gary, R. Barat, F. Oliveira, and D. Zimdars, "THz imaging and sensing for security applications—explosives, weapons and drugs," Semiconductor Science and Technology **20**, S266 (2005).

[37] European Commission, "Towards a more secure society and increased industrial competitiveness," (2009).

[38] A. J. Fitzgerald, E. Berry, N. N. Zinovev, G. C. Walker, M. A. Smith, and J. M. Chamberlain, "An introduction to medical imaging with coherent terahertz frequency radiation," Physics in Medicine and Biology **47**, R67 (2002).

[39] B. Ferguson, S. Wang, D. Gray, D. Abbot, and X.-C. Zhang, "T-ray computed tomography," Optics Letters **27**, 1312–1314 (2002).

[40] T. Paoli and J. Ripper, "Direct modulation of semiconductor lasers," Proceedings of the IEEE **58**, 1457–1465 (1970).

[41] K. Y. Lau, J. Park, O. Solgaard, and K. J. Vahala, *Ultra-high frequency linear fiber optic systems*, vol. 159 (Springer, 2011).

[42] A. Laakso and M. Dumitrescu, "Modified rate equation model including the photon–photon resonance," Optical and Quantum Electronics **42**, 785–791 (2011).

[43] J.-F. Lepage and N. McCarthy, "Analysis of dual-wavelength oscillation in a broad-area diode laser operated with an external cavity," Applied Optics **41**, 4347–4355 (2002).

[44] Z. Gao, L. Wang, and J.-J. He, "Mode competition analysis in dual-wavelength coupled-cavity semiconductor laser," Journal of the Optical Society of America B **27**, 432 (2010).

[45] K. J. Vahala, M. A. Newkirk, and T. R. Chen, "The optical gain lever: A novel gain mechanism in the direct modulation of quantum well semiconductor lasers," Applied Physics Letters **54**, 2506–2508 (1989).

[46] S. O'Brien, S. Osborne, D. Bitauld, N. Brandonisio, A. Amann, R. Phelan, B. Kelly, and J. O'Gorman, "Optical synthesis of terahertz and millimeter-wave frequencies with discrete mode diode lasers," IEEE Transactions on Microwave Theory and Techniques **58**, 3083–3087 (2010).

[47] S. O'Brien, S. Osborne, K. Buckley, R. Fehse, A. Amann, E. P. O'Reilly, L. P. Barry, P. Anandarajah, J. Patchell, and J. O'Gorman, "Inverse scattering approach to multiwavelength fabry-pérot laser design," Phys. Rev. A **74**, 063814 (2006).

[48] P. Zory, *Quantum Well Lasers*, OPTICS AND PHOTONICS SERIES (Academic Press, 1993).

[49] G. Agrawal, "Gain nonlinearities in semiconductor lasers: Theory and application to distributed feedback lasers," Quantum Electronics, IEEE Journal of **23**, 860–868 (1987).

[50] A. E. Siegman, *Lasers* (1986).

[51] R. Czarny, M. Alouini, C. Larat, M. Krakowski, and D. Dolfi, "THz-dual-frequency Yb3+:KGd(WO4)2 laser for continuous wave THz generation through photomixing," Electronics Letters **40**, 942–943 (2004).

[52] G. Baili, L. Morvan, M. Alouini, D. Dolfi, F. Bretenaker, I. Sagnes, and A. Garnache, "Experimental demonstration of a tunable dual-frequency semiconductor laser free of relaxation oscillations," Optics Letters **34**, 3421–3423 (2009).

[53] N. Kim, J. Shin, E. Sim, C. W. Lee, D.-S. Yee, M. Y. Jeon, Y. Jang, and K. H. Park, "Monolithic dual-mode distributed feedback semiconductor laser for tunable continuous-wave terahertz generation," Optics Express **17**, 13851–13859 (2009).

[54] I. Sahl, *On Burning Mirrors and Lenses* (984).

[55] C. Huygens, T. Young, A. J. Fresnel, and F. Arago, *The wave theory of light: memoirs of Huygens, Young and Fresnel* (American Book Company, 1900).

[56] E. Hecht, *Optics* (Addison Wesley, 2001), 4th ed.

[57] P. Yeh, *Optical waves in layered media*, vol. 95 (Wiley New York, 1988).

[58] L. Zhang, S. Yu, M. Nowell, D. Marcenac, J. Carroll, and R. Plumb, "Dynamic analysis of radiation and side-mode suppression in a second-order DFB laser using time-domain large-signal traveling wave model," IEEE Journal of Quantum Electronics **30**, 1389–1395 (1994).

[59] A. Akrout, K. Dridi, S. Abdul-Majid, J. Seregelyi, and T. Hall, "Numerical study of dual mode generation using a sampled-grating high-order quantum-dot based laterally-coupled DFB laser," IEEE Journal of Quantum Electronics **49**, 821–828 (2013).

[60] B. R. Bennett, R. A. Soref, and J. A. Del Alamo, "Carrier-induced change in refractive index of InP, GaAs and InGaAsP," IEEE Journal of Quantum Electronics **26**, 113–122 (1990).

[61] J. A. McCaulley, V. M. Donnelly, M. Vernon, and I. Taha, "Temperature dependence of the near-infrared refractive index of silicon, gallium arsenide, and indium phosphide," Physical Review B **49**, 7408–7417 (1994).

[62] H. Kogelnik and C. V. Shank, "Coupled-Wave theory of distributed feedback lasers," Journal of Applied Physics **43**, 2327 (1972).

[63] J. Maxwell Clerk, "A dynamical theory of the electromagnetic field." Proceedings of the Royal Society of London **13**, 531–536 (1863).

[64] A. Laakso, M. Dumitrescu, J. Viheriälä, J. Karinen, M. Suominen, and M. Pessa, "Optical modeling of laterally-corrugated ridge-waveguide gratings," Optical and Quantum Electronics **40**, 907–920 (2009).

[65] W. Streifer, R. Burnham, and D. Scifres, "Effect of external reflectors on longitudinal modes of distributed feedback lasers," IEEE Journal of Quantum Electronics **11**, 154– 161 (1975).

[66] H. Ghafouri–Shiraz, *Distributed Feedback Laser Diodes and Optical Tunable Filters* (John Wiley & Sons, Ltd, 2003).

[67] J. A. Nelder and R. Mead, "A simplex method for function minimization," The Computer Journal **7**, 308–313 (1965).

[68] A. Laakso, J. Karinen, J. Telkkälä, and M. Dumitrescu, "The effect of facet reflections in index-coupled distributed feedback lasers with coated facets," Optical and Quantum Electronics **42**, 713–719 (2011).

[69] K. E. Parsopoulos and M. N. Vrahatis, "Particle swarm optimization method in multiobjective problems," in "Proceedings of the 2002 ACM Symposium on Applied Computing," (ACM, New York, NY, USA, 2002), SAC '02, p. 603–607.

[70] A. D. Bethke, "Genetic algorithms as function optimizers," (1978). `http://deepblue.lib.umich.edu/bitstream/2027.42/3572/5/bab2694.0001.001.pdf`.

[71] Y. Jin, M. Olhofer, and B. Sendhoff, "Dynamic weighted aggregation for evolutionary multi-objective optimization: Why does it work and how?" .

[72] P. J. Fleming and A. P. Pashkevich, "Computer aided control system design using a multiobjective optimization approach," Control 85 pp. 174–179 (1985).

[73] L. A. Coldren, S. W. Corzine, and M. L. Mashanovitch, *Diode lasers and photonic integrated circuits*, vol. 218 (John Wiley & Sons, 2012).

[74] G. Chen, S. R. Seshadri, and F. Cerrina, "Distributed feedback lasers with distributed phase-shift structure," Applied Physics Letters **60**, 2586–2588 (1992).

[75] G. P. Agrawal, J. E. Geusic, and P. J. Anthony, "Distributed feedback lasers with multiple phase-shift regions," Applied Physics Letters **53**, 178–179 (1988).

[76] C. S. Inc., "Pics3d, photonic integrated circuit simulator in 3d," (2013).

[77] J. Boavida, J. Morgado, and C. Fernandes, "HR-AR coated DFB lasers with high-yield and enhanced above-threshold performance," Optics & Laser Technology **43**, 729–735 (2011).

[78] J. Kinoshita and K. Matsumoto, "Yield analysis of SLM DFB lasers with an axially-flattened internal field," IEEE Journal of Quantum Electronics **25**, 1324–1332 (1989).

[79] J. Sun, Y. Dai, X. Chen, Y. Zhang, and S. Xie, "Stable dual-wavelength DFB fiber laser with separate resonant cavities and its application in tunable microwave generation," IEEE Photonics Technology Letters **18**, 2587 –2589 (2006).